Journal of Structural Geology 180 (2024) 105058

Contents lists available at ScienceDirect

Journal of Structural Geology

journal homepage: www.elsevier.com/locate/jsg

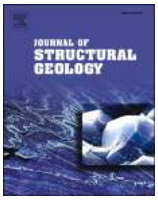

Seismic faulting and CO2-rich fluid interactions: Evidence from carbonate spherulitic grains in ultramafic fault damage zones

Michele Locatelli [a], Laura Crispini [a,*], Elisabetta Mariani [b], Giovanni Capponi [a], Marco Scarsi [a], Laura Federico [a]

[a] Department of Earth, Environment and Life Sciences (DISTAV), University of Genoa, Corso Europa 26, Genoa, Italy
[b] University of Liverpool, Department of Earth, Ocean and Ecological Sciences, 4 Brownlow Street, Liverpool, United Kingdom

ARTICLE INFO

Keywords:
Carbonated ultramafics
Fault rocks
Fluid rock interaction
Seismic faults
Spherulites
Clast cortex aggregates
Voltri Massif

ABSTRACT

Faults and shear zones in the metamorphic ultramafic rocks of the Voltri Massif (Ligurian Alps, NW Italy) are often accompanied by intense or complete carbonation of the host rocks. One of these fault zones, hosted in peridotite and serpentinite, is characterized by distinctive structural features that can be related to a fluid-assisted multistage brittle deformation, indicative of paleoseismic activity. The fault rocks contain cataclasite and breccias with layers of coseismic spherulitic grains of dolomitic composition, silica/calchedony veins and cement, and saponite bearing gouge. The fault is part of a system of regional structures associated with gold mineralization in quartz veins and various stages of hydrothermal alterations.

Here we present a multiscale study of this fault zone combining field observations, microstructural analysis, SEM-EDS, and electron backscattered diffraction (EBSD). Focus is on the microstructures of the fault core and the significance of the characteristic carbonate spherulite layers in association with silica/chalcedony cement and veins. Our results show that these structures are indicative of the interaction between CO_2-rich fluids released during coseismic and interseismic phases of faulting, i.e., during cycles of fluid pressure build-ups, faulting, fluid flushing, and mineral precipitation and sealing during seismic failure of the fault.

1. Introduction

Exhumed fault zones represent an engaging research topic due to the important information they provide on processes controlling rock deformation, crustal fluid migration, and seismic activity (Faulkner et al., 2010; Sibson, 1977, 1992, 2001; Sibson et al., 1988). Fault zones may act as barriers, conduits, or even as pumps and valves during cycles of deformation in the brittle-viscous, seismogenic region of the crust (Shelly et al., 2015; Sibson, 1981, 1992; Sibson et al., 1988). The development of fault zones within crustal rock piles, and the mechanisms whereby they weaken and fail, are complex functions of a number of processes, among which fluid-mineral interactions at the fault core may play a major role (Kaduri et al., 2017). In particular, fault zones developed within serpentinites are of great interest because some authors suggest that they do not develop seismic structures, but rather creep aseismically during shear deformations (Moore and Lockner, 2013). Such creeping faults display similar mechanical behavior to those developed in carbonates, which experience mineral dissolution during fast slip, with significant fault weakening (e.g., Rowe et al., 2012; Rogowitz et al., 2016).

In regions of the crust where faulting is accompanied by significant flow of hydrothermal fluids, failure and comminution processes increase the reactive surface of rocks and promote the generation of hydrothermal alteration haloes adjacent to the rock volume where failure occurs (Reed, 1997). This metasomatic process, which is controlled by advection and diffusion, influence mineral precipitation in the fault zone (Cathles, 1991) and is important not only because it may control location, emplacement, and volumetric extent of economic mineral deposits and geothermal systems (Caine and Forster, 2013; Micklethwaite, 2009; Sibson, 2001), but also because it may affect the seismicity of the upper crust (Gudmundsson et al., 2010).

Metasomatic processes taking place during infiltration of CO_2-rich fluids in ultramafic rocks lead to intense exothermal carbonation (e.g., Kelemen et al., 2011; van Noort et al., 2013; Herviou and Bonnet, 2023;

* Corresponding author. Department of Earth Sciences, Environment and Life (DISTAV), University of Genoa, C.so Europa 26, 16132 Genoa, Italy.
E-mail addresses: michele.locatelli@edu.unige.it (M. Locatelli), laura.crispini@unige.it (L. Crispini), mariani@liverpool.ac.uk (E. Mariani), capponig@gmail.com (G. Capponi), marko.scarsi@gmail.com (M. Scarsi), laura.federico@unige.it (L. Federico).

https://doi.org/10.1016/j.jsg.2024.105058
Received 17 October 2023; Received in revised form 23 December 2023; Accepted 6 January 2024
Available online 17 January 2024

Piccoli et al., 2016; Hu et al., 2021). Such processes generate the gamut of carbonated rocks, that include listvenites (quartz-carbonate-fuchsite assemblage), quartz-carbonate rocks (silica-carbonate assemblage), serpentine-talc-carbonate-(chlorite) rocks, and others; such rocks, and above all the listvenites, are long known to be genetically linked with orogenic gold mineralizations (e.g., Belogub et al., 2017; Halls and Zhao, 1995).

Many studies show that during seismic faulting, the initial failure depends both on the frictional resistance of fault planes and on fault lubrication (see review in: Di Toro et al., 2011; Niemeijer et al., 2012). Lubrication consists of a set of physical and chemical processes that significantly decrease the frictional strength of a fault and includes flash heating of fault asperities, frictional melting (pseudotachylytes), formation of amorphous silica and nano-powder, and thermal decomposition (e.g., Di Toro et al., 2011). Such processes act during earthquakes at all crustal levels, irrespective of fault rock composition, but their role is complex and not documented in detail. Studies support the idea that several lubrication mechanisms may act simultaneously in the crust allowing fault slip (see discussion in Di Toro et al., 2011, 2006; Niemeijer et al., 2012), but the persistence and efficiency of these processes are still unknown. In the shallowest section of the crust findings of pseudotachylytes are extremely rare (e.g., Otsuki et al., 2009; Lin, 1994; Swanson, 1988) and only recently were reported the findings of glassy pseudotachylytes formed at depths <1 km (e.g., the melted gouges of the MW 7.9 Wenchuan earthquake; Wang et al., 2023). Aside the devitrification of glassy material under typical geological conditions (e.g., Kirkpatrick and Rowe, 2013; Fondriest et al., 2020), the scarcity of pseudotachylytes in shallow crust (e.g., Otsuki et al., 2009; Wang et al., 2023; Lin, 1994) can be ascribed to alternative lubrication processes (Kuo et al., 2016), some of which involving hydrothermal fluids (Brodsky and Kanamori, 2001).

This claim leads to the conclusion that pseudotachylytes are not the sole seismic indicators found in rocks, and that other seismic structures can develop, although no general consensus exists on their interpretation. Accordingly, additional indicators could be mirror-like slip surfaces (Fondriest et al., 2012; Evans et al., 2014; Kuo et al., 2016; Rowe and Griffith, 2015), clast-cortex aggregates (Rempe et al., 2014; Rowe and Griffith, 2015; Smith and Faulkner, 2010; Smith et al., 2011; Kim et al., 2022), layers of amorphous silica (Kirkpatrick et al., 2013; Aretusini et al., 2017), and pulverized rocks or fluidized gouges (Yuan et al., 2011).

In this work, we focused on a thrust fault zone exposed along the Bisciarelle Creek (Ligurian Alps, Italy, Fig. 1); we combined field data, microtextural data, SEM-energy dispersive X-ray spectroscopy (EDS), and electron backscattered diffraction (EBSD), in order to constrain (i) fluid-rock interaction in the damage zone, (ii) deformation and fluids pathways in the fault core, (iii) potential paleo-seismic indicators and (iv) to model the structural evolution of this brittle fault zone.

2. Study area

The study area is located in the northern part of the Voltri Massif (Ligurian Alps, that are the southernmost part of the Western Alps, NW Italy), in the Lavagnina Lakes area (Fig. 1). The Lavagnina Lakes rocks mostly consist of serpentinites associated with metagabbros, metabasites, metasediments, and metaperidotites (i.e., metamorphic lherzolites plus minor pyroxenites and dunite bodies; Fig. 1a and b), which are attributed to the tectonometamorphic Voltri Unit (Capponi et al., 2016; Scarsi, 2018). The metamorphic rocks are unconformably covered by the syn to post-orogenic continental breccias and conglomerates of the Tertiary Piedmont Basin (age: upper Eocene – lower Oligocene; Gelati and Gnaccolini, 1988).

The Voltri Unit underwent a complex Alpine tectonic and metamorphic history, spanning from ductile to brittle regimes (e.g.; Capponi and Crispini, 1997; Capponi and Crispini, 2002) and experienced high-pressure metamorphic conditions variably re-equilibrated in

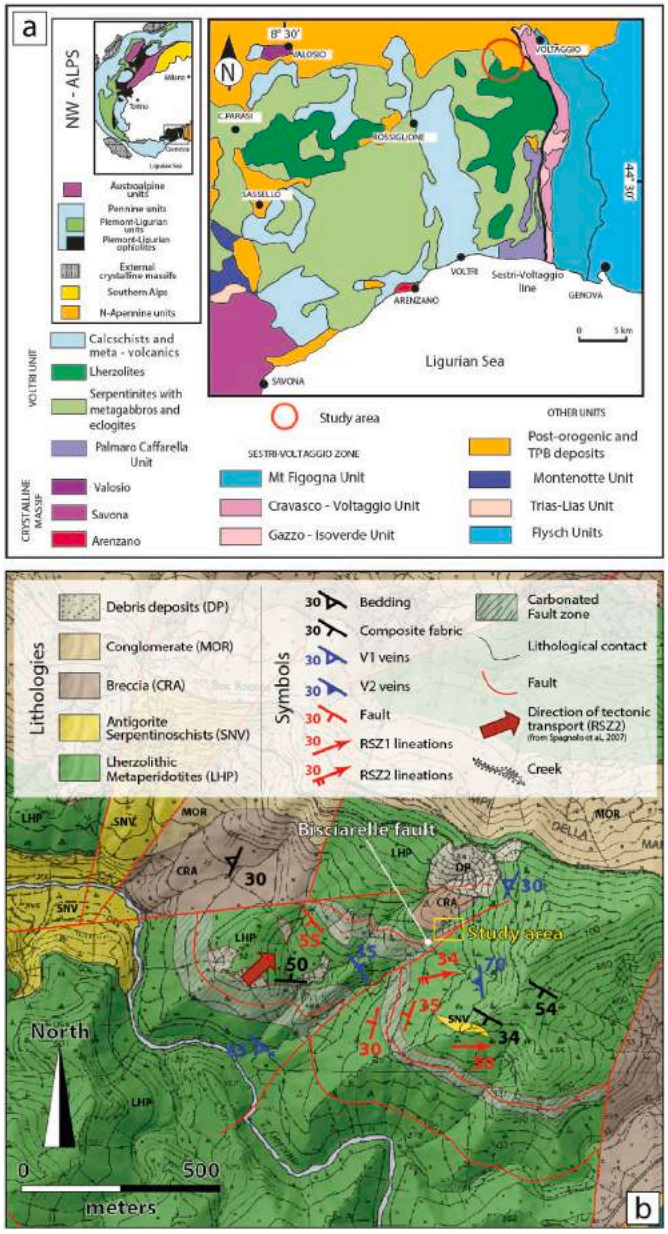

Fig. 1. Geological and geographical setting of the study area. (a) Structural map of the eastern Ligurian Alps and adjoining units (after: Capponi and Crispini, 2002), and structural sketch map of the Western Alps (inset at the top left). (b) Detailed geological map of the study area and location of the Bisciarelle fault (with modifications from Scarsi et al., 2019). The direction of tectonic transport is derived from Spagnolo et al. (2007).

greenschist facies (Cimmino and Messiga, 1979; Messiga & Scambelluri, 1991 Capponi and Crispini, 1997; Desmons et al., 1999; Scarsi, 2018). Late Alpine orogenic events (Late Eocene-Early Miocene) were characterized by superposed syn-metamorphic and non-metamorphic structures, mainly linked to a compressional/transpressional tectonics active at the regional scale (e.g., Capponi and Crispini, 2002; Maino et al., 2013; Morelli et al., 2022; Manna et al., 2023; Mueller et al., 2023) that eventually conditioned the quaternary morphostractural setting of the Ligurian Alps (Morelli et al., 2023). Interested readers are referred to a specific literature for a more comprehensive documentation of the tectonic and geologic evolution of the area (e.g.; Capponi et al., 1998, Capponi et al., 2016; Pipino, 2003; Spagnolo et al., 2007; Crispini et al., 2009; Scarsi et al., 2019; Vignaroli et al., 2010; Smye et al., 2021). In the Lavagnina Lakes zone (Fig. 1b) ultramafic rocks are dominantly

meta-lherzolites and harzburgites partially to completely affected by serpentinization, with subordinated lenses of dunite and metagabbros and metabasites (e.g., Scambelluri et al., 1991; Cannaò et al., 2016). Sedimentary deposits are in contact with the metamorphic basement along transgressive unconformities or faults (Capponi et al., 1998, Fig. 1b).

A complex series of superimposed deformational events, related to ductile to brittle-ductile to pure brittle tectonic regimes, have been recorded in the study area (Spagnolo et al., 2007). The oldest Alpine structures are characterised by folds and a composite, pervasive foliation that controls the limits among the lithologies at the mesoscale (D1-D2 deformation phases of Capponi and Crispini, 2002). The subsequent deformation events developed at higher structural levels and are represented by different set of folds (cf. D3 and D4 folds of Capponi and Crispini, 2002), reverse shear zones, and fault systems (Spagnolo et al., 2007; Federico et al., 2009, 2014; Crispini et al., 2009). Brittle-ductile, upper crustal deformations are common in the study area (Spagnolo et al., 2007) as evidenced by the occurrence of sets of Reverse Shear Zones (RSZ, hereafter; Fig. 1b) which develop vein networks, wall rock metasomatic alterations, and local gold mineralization in quartz veins (see Pipino, 2003). According to their structural features and kinematics, the RSZ have been divided into two distinct crosscutting deformational events. The older RSZ1, develops ductile to brittle-ductile structures syntectonic with greenschist to sub-greenschist metamorphic conditions. The younger RSZ2 develops top-to-E/NE brittle-ductile to pure brittle structures formed at sub-greenschist to zeolite facies metamorphic conditions. The damage zones of the RSZ2 host gold-bearing quartz + carbonate veins and chalcedony veins (V2 and V3 of Spagnolo et al., 2007), in addition to hydraulic breccia and cockade breccia. The fault object of this paper (i.e., the Bisciarelle fault) has been ascribed to the Au bearing RSZ2 system (Spagnolo et al., 2007) and the D4 tectonic event of the Voltri Massif (late Oligocene-early Miocene, Capponi and Crispini, 2002; Spagnolo et al., 2007). It has been first mapped by Spagnolo et al. (2007) and studied by Scarsi (2018), Scarsi et al. (2019) and Garofalo et al. (2023). More detail about it structural setting are presented below in paragraph §3 “Results”.

3. Methods

In this work we present the structural/microstructural characterization of the Bisciarelle fault Zone (Fig. 1b) achieved through detailed fieldwork and sampling of both the fault damage zone and the ultramafic host rock (Fig. 2a and b). The geochemical insights deciphering the fluid/rock interaction along the Bisciarelle fault zone are presented in the companion paper of Garofalo et al. (2023).

The microstructural and petrographic study of the fault core is based on 18 rock samples (i.e., carbonated cataclasite, spherulite layers, breccias, and gouges; cf. Fig. 2c) collected to define the deformation history and the strain gradient across the fault (Fig. 2c). In addition, a set of 10 samples from a transect across the serpentinized lherzolite host-rock and the damage zone was collected to study the feedback between hydrothermal fluid flow and metal transport within carbonated ultramafics (see Garofalo et al., 2023). All the samples were used to carry out a multi-technique analytical documentation of fault zone and host rock, which includes (in addition to field structural data), petrography, SEM-energy dispersive X-ray spectroscopy (EDS) and electron backscattered diffraction (EBSD). Microtextural and petrographic study and SEM-EDS analyses were carried out at the University of Genova (Department of Earth, Environment and Life Sciences – DISTAV). Two thin sections (M1E and MP215) and two large individual spherulites (~10 mm diameter), manually separated from the matrix, were polished to high quality for EBSD using diamond polishing medium down to 0.24 μm particle size. Chemo-mechanical polishing was then carried out using colloidal silica (0.05 μm silica particle size suspended in an alkaline solution) to remove the amorphous surface layer that forms due to a degree of surface damage during mechanical polishing. All samples are non-conductive and therefore a thin carbon coat (10–30 nm) was applied to avoid electron accumulation and consequent charging effects during analyses. EBSD analyses were carried out at the University of Liverpool using the CamScan X500 Crystal Probe field emission gun (FEG) SEM in the EBSD-SEM Laboratory (School of Environmental Sciences), now part of the University-wide Scanning Electron Microscopy Shared Research Facility (SEM SRF). Electron backscatter diffraction patterns (EBSPs) were obtained via a Nordlys EBSD detector, using 20 kV accelerating voltage, 35 nA beam current and 25 mm working distance. EBSPs were automatically indexed and then analyzed using the free, open source MatLab toolbox MTEX (Bachmann et al., 2010). EBSD measures the absolute crystallographic orientation of any crystalline material (Prior et al., 1999, 2009; Mariani et al., 2009). In this study the microstructure of a number of spherulites, ranging in size from few 100 μm to 10 mm was reconstructed by calculating the orientation difference (disorientation) between neighboring data points. Errors on orientation measurements are within ±0.5°. To achieve best results, EBSD grid spacing (step size), and the size of areas analyzed were varied as a function of spherulite size.

Results of chemical analyses by laser ablation-inductively coupled plasma-time-of-flight mass spectrometry (LA-ICP-TOFMS) on the same samples are described by Garofalo et al. (2023).

4. Results

4.1. Structural data

In the study area (Fig. 1), the Bisciarelle fault zone is exposed for about 100 m in length and nucleates inside serpentinized peridotites (Fig. 2a and b) at the contact between meta-lherzolites and serpentinites (Fig. 3a-c). This is an irregular, not-planar reverse fault, low-to-moderate W-SW-dipping with top-to-NE sense of shear (Fig. 2a and b). The fault zone is 19 m-thick, has an asymmetric damage zone that is thicker at the footwall, and is made of fault gouge, cataclasites, and ultracataclasites (Fig. 2c; Scarsi 2018; Scarsi et al., 2019).

At the footwall, the host rock consists mainly of partially serpentinized lherzolite with minor dunite and pyroxenite (Fig. 2b). Meta-lherzolite preserves either mantle foliations or metamorphic foliations linked to the orogenic HP-LT deformations.

4.1.1. Fault zone anatomy

The fault zone can be divided into i) hanging wall damage zone, ii) fault core, and iii) footwall damage zone (Fig. 2b and c). The damage zone is here considered as the section of the fault with relatively low strain, less intense deformation, and hosting subsidiary veins (inset of Fig. 2b). It can be classified as a “wall damage zone” or an “along-fault damage zone” according to current classifications (Choi et al., 2016; Kim et al., 2004).

The transition from the host rock to the hanging wall damage zone is marked by a systematic change of color and veinlet density (Fig. 2b and c), which provide evidence for rock metasomatism and brittle deformation progressively more intense towards the fault core.

i) Hanging wall damage zone

The hanging wall is made mainly of a serpentinite schist with relics of lherzolite. Serpentinite has a penetrative foliation, parallel to the fault core (Fig. 2b); it is brown (serpentinite schist) to green (metasomatized layers) in color, depending on the relative abundance of the secondary metasomatic minerals. Serpentinite-schist are arranged in duplex structures and phacoid-shaped lenses with polished surfaces or surfaces coated by serpentine fibres (inset of Fig. 2b). Phacoids are bounded by poorly cohesive fault gouges, which host a system of extensional carbonate veins (e.g., the “carbonated fault gauge with veins”, cfr. Fig. 2c; see par. §4.2.1). The veins that crosscut the serpentinite schist foliation at high angle are on average 2–3 cm thick; whereas those developed sub-

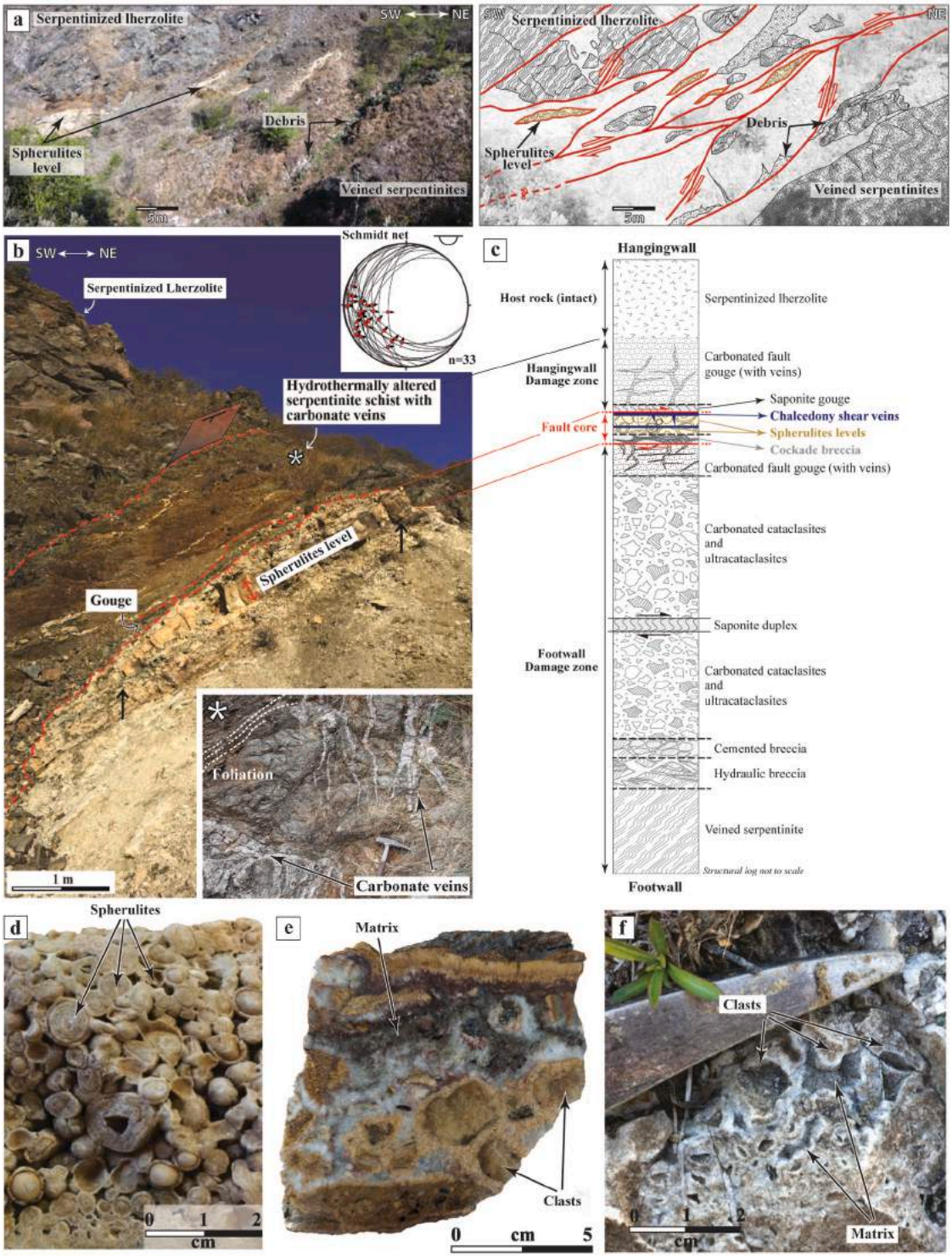

Fig. 2. Field appearance of the Bisciarelle fault zone. a) Outcrop photography of the Bisciarelle fault zone, with the serpentinite schists arranged in duplex structures. The Spherulites-bearing layers are highlighted in yellow. (b) Field appearance of the hanging wall of the Bisciarelle fault, with the abundant debris generated by surface erosion which cover most of the footwall elements of the fault. The vertical black arrows mark the end-tips of the spherulite layer, which thickness is highlighted by the red arrow. The asterisk marks the location of the hydrothermally altered serpentinite schists, which display two main sets of carbonate-bearing veins that crosscut the foliation, both at high angle (e.g., sub-perpendicularly, thickness: ~2–3 cm) and sub-parallel (thickness up to 20 cm). Locally, smaller, mm-scale veinlets may cut the serpentinite foliation at an angle of 15–20°. In the inset is reported the stereoplot (Schmidt net, lower hemisphere) of the Bisciarelle fault surfaces (the arrows show the slickenlines top-to directions). (c) Structural log (not to scale) summarizing the complex internal structure of the Bisciarelle thrust fault. Spherulite layers formed at the fault core are enlightened in yellow, chalcedony shear veins in blue. (d) Field appearance of the spherulite-rich layer, characterized by mm-sized, spherical and highly-rounded dolomite spherulites. (e) Detail of a cockade breccia polished slab displaying the characteristics cm-sized angular clasts surrounded by concentric layers of yellow-tinted, calcite-rich cement. Voids are filled by a matrix consisting of geopetals made of greenish, euhedral carbonates (e) Field appearance of a cockade breccia layer, developed at the base of the fault core. Clasts (up to 50% of the layer volume) are made of angular to sub-angular serpentinite and carbonated serpentinite. The greenish matrix consisting of geopetals made of euhedral carbonates is here well visible.

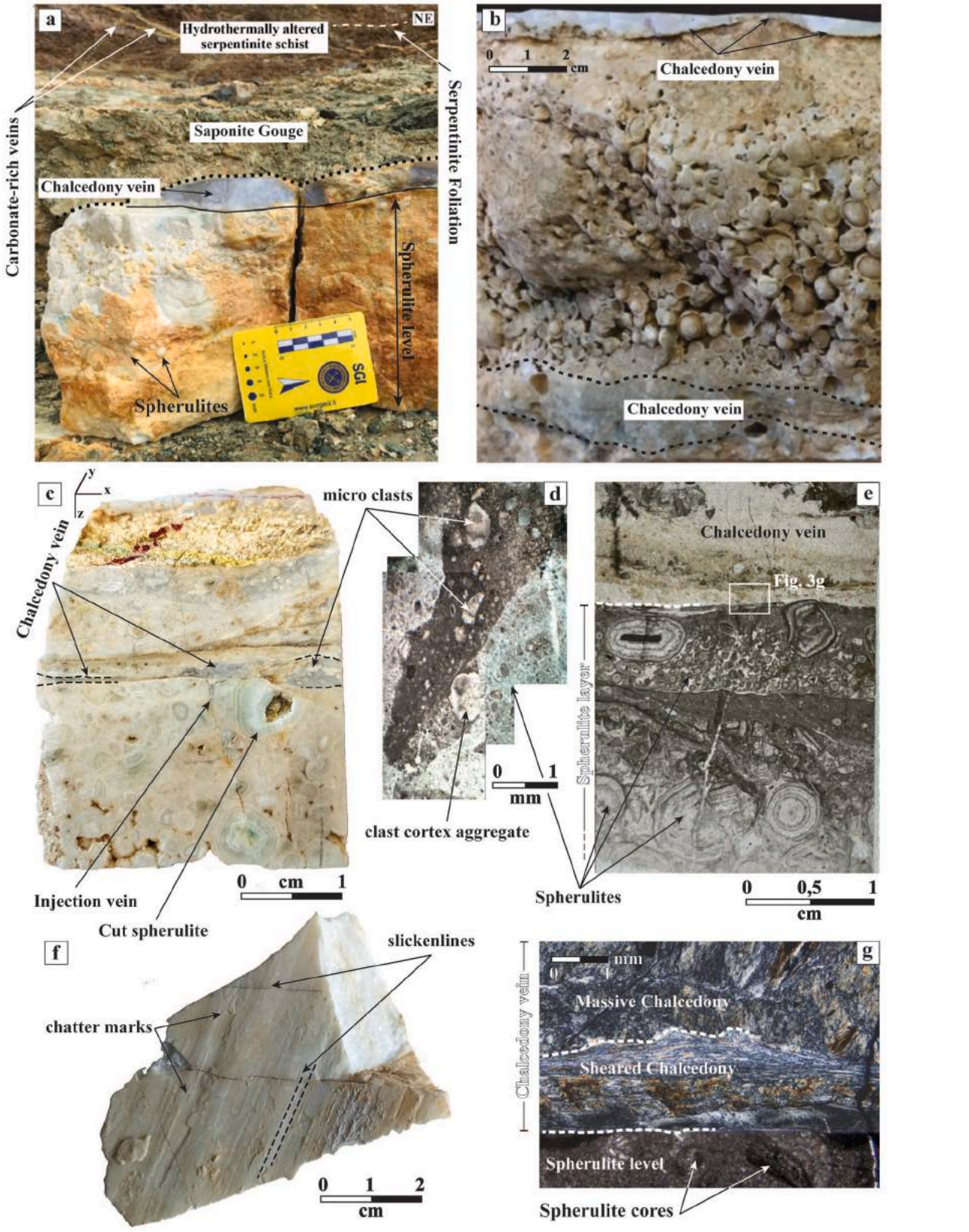

(caption on next page)

Fig. 3. Appearance of the spherulite-rich layers. (a) Contact between a spherulite layer and the saponite-carbonate gouge of the hanging wall, marked by a cm-thick calcedony shear vein. Individual spherulites may reach centimetric dimensions (up to 1 cm in diameter) and are generally close packed. The different outcrops colours marks the degrees of watering, from high (yellow/orange tints) to low/absent (whitish/pale green). (b) spherulite sample showing the high porosity of the layer, linked to late-stage watering of the cement precipitated around the spherulites. Locally, the concentric texture of single spherulites is visible. c) Polished rock slab of a spherulite-rich layer. It is evident how the concentric textures are typical for larger spherulites, while the smaller are generally massive. Here the calcedony shear veins (grayish color) sharply crosscut the spherulites and develop millimeter-scale injection veins, which are interspersed by micrometric fragments of spherulites, clast-cortex aggregates and host-rock. (d) Detail of a chalcedony injection vein. The dark color of the vein's bulk is given by the micro-fragments of the host-rock and oxides interspersed in the chalcedony cement. Plane polarized light microphotograph. (e) Panoramic thin section showing the transition between a chalcedony vein and a spherulites-rich layer, which also host clast-cortex aggregates. Different cores can be recognized inside the bigger spherulites (e.g., fragments of the serpentinite host-rock or older spherulites aggregates). Multiple stages of spherulites growth and brittle deformation can be recognized. Plane polarized light microphotograph. (f) Unpolished slab of chalcedony vein, with preserved slickenlines and chatter marks. (g) Detail of the transition between a spherulites-rich layer and a chalcedony vein. This latter grows chalcedony slick fibres sub-parallel to the vein wall. Cross polarized light microphotograph.

parallel to foliation are thicker (up to 20 cm; Fig. 2b and c). Locally, smaller, mm-scale veinlets cut the serpentinite foliation at an angle of 15–20°. The transition to the fault core is marked by a major layer of fault gouge which consists of a ~50 cm thick level made of carbonate and emerald-green saponite ("saponite gouge", cfr. Figs. 2b, c and 3a).

ii) Fault core

The fault core is ~70 cm thick and displays a great compositional and structural complexity. It shows several parallel multiphase slickensides (Fig. 2b), sub-horizontal or gently dipping to W, with marked slickenlines and grooves that dip to W-SW (box in Fig. 2b). Stretching lineations and kinematic indicators indicate a main top-to E/NE direction of tectonic transport (Schmidt net of Fig. 2a, modified from Garofalo et al., 2023) with an overall, major reverse slip component coupled with a minor strike slip component.

Moving from the top to the bottom of the fault core, various, decimeter-thick, structural layers have been recognized (Fig. 2c, see also Scarsi, 2018), respectively: (a) dolomitic "spherulites" and minor clast cortex aggregates, (b) chalcedony shear veins, (c) injection veins, and (d) cockade breccias.

The two layers containing the (a) spherulites (*sensu* Shtukenberg et al., 2012) are found at the contact with the hanging wall and consist of ~10–20 cm-thick, whitish in colour, highly porous levels that are continuous for several meters in length (Fig. 2a-c). Here, spherulites crystallize as sub-spheric grains (Fig. 2d) made of ferroan dolomite and display a distinct concentric texture visible both at the outcrop scale (Figs. 2d and 3a-c) and microscale (Fig. 3d and e). Spherulites occupy up to 80% of the rock volume and their size ranges between 1 mm and 1.8 cm. Minor clast-cortex aggregates (less than 2% of the rock volume) are also observed at the contact between spherulite layers and (b) chalcedony veins (e.g., Fig. 3e). These latter are abundant (Fig. 3a-g) and locally develop extremely smooth and polished surfaces (i.e., slip zones with slickenlines and chatter marks that can be considered as mirror surfaces, *sensu* Evans et al., 2014; Rowe and Griffith, 2015, Fig. 3f) which cut the spherulites layers, displaying a top-to-NE sense of shear. Such milky/greyish in color chalcedony shear veins have maximum thickness of 10–15 mm, show distinct flow banding-like textures (cf. Faber et al., 2014) and can either contain fragments of host-rock and spherulites (up to 10–20% of the vein volume), Fig. 3c) or be entirely made of chalcedony (Fig. 3a, b, e). The occurrence of intense comminution of spherulites-rich host-rock (fragments size down to 0.5 mm; Fig. 3c) and contemporary rotation/overgrowth of single spherulites along the chalcedony slip surfaces unequivocally indicate that the processes of spherulites growth and shear deformation were coeval. Towards the top of fault core, the above-described structures are crosscut by injection-veins (see also Garofalo et al., 2023) irradiating from the outermost part of the chalcedony-veins, which mark the transition between the fault core and the gouge of the hanging-wall damage zone (Fig. 3a and b). These injections (Fig. 3c and d) have thickness of few millimetres and host angular to sub-angular fragments of carbonate clasts (sizes: up to 1.5 mm; ~10 vol %), spherulites and clast cortex aggregates (sizes: up to 0.5 mm; ~10–15 vol %, Fig. 3d) in a matrix of chalcedony or fine-grained quartz.

Towards the footwall, spherulite-rich layers are bound by ~20 cm-thick, unaltered and undeformed layers made of cockade breccias (cf. Genna et al., 1996; Frenzel and Woodcock, 2014; Cox and Munroe, 2016; Berger and Herwegh, 2019). With respect to the spherulites, the core clasts of these breccias are angular and centimetric in size (Fig. 2e and f) and are made of serpentinite and carbonated serpentinites. Clasts occupy up to 50% of the rock volume and the matrix consist of geopetal structures made of euhedral carbonates (Fig. 2e). Close to the footwall, the breccia shows an increase in clast dimensions and a concomitant decrease in carbonate matrix.

iii) Footwall damage zone

The ~8 m-thick footwall damage zone (Fig. 2c) is lithologically and structurally composite. It encompasses, from the top to the bottom: (i) carbonated fault gouge with veins (~1 m thick); (ii) carbonated cataclasites and ultracataclasites (~5 m thick) intercalated with saponite/serpentinite bearing duplex layers (~ 10–15 cm thick); (iii) cemented breccias (<0.5 m thick), (iv) hydraulic breccias (~1 m thick) and (v) veined serpentinite and serpentinite schists.

The carbonated fault gouge (cf. Sibson, 1977), green in colour, is made of serpentinite clasts randomly oriented within a carbonate-rich serpentinite matrix. The transition towards the carbonated cataclasites (dark-green in colour) and the ultracataclasites (brownish in colour) is marked by the increase in size of the clasts (made of randomly oriented, angular serpentinite fragments with sizes <1 cm). These are surrounded by a microcrystalline, soft and red carbonate matrix, which became progressively more competent towards the footwall (i.e., the cemented breccias). The pale-green hydraulic breccias (cf. Genna et al., 1996) mark the transition to the veined serpentinites; they have maximum thickness of ~30 cm and contain coarse (1–10 cm in size), angular to sub-angular serpentinite clasts cemented by whitish carbonate matrix.

The lithologies of the footwall damage zone host several systems of extensional veins, randomly oriented across the schistosity. These cm-thick veins, filled by elongate, blocky to fibrous calcite crystals and chalcedony cut the regional schistosity and are, in turn, cut by two types of sigmoidal duplex structures (cf. Ramsay and Huber, 1987, Fig. 2c), both indicating a top-to-NE sense of shear.

We emphasize that the structural elements described above are cut by R-Shear fractures (Ramsay and Huber, 1987), which are NNW-SSE striking, dipping at relatively high angles (40–60°), and showing a top-to-NE direction of tectonic transport. In the central part of the fault core, they dissect the spherulite layers in at least 4 slices.

In summary, all the structural elements of the reverse Bisciarelle fault zone show a consistent top-to-NE- or E direction of tectonic transport, with multiple reactivation events under brittle deformation conditions in a fluid-rich environment.

4.2. Microstructures

In the following sections, we report microstructural characteristics and petrographic data separately for host rock and fault core.

4.2.1. Host rock

Away from the hanging wall damage zone (~16 m from the fault core), the relic protolith within the host rock shows the typical assemblage of the Voltri Massif meta-lherzolite, i.e. orthopyroxenes, clinopyroxenes, olivine and spinel (Fig. 4a), and are characterised by a tectonitic or mylonitic mantle foliation (Scambelluri et al., 2001). Mantle assemblages and foliations are partially to completely overprinted by secondary serpentine minerals in mesh textures (Fig. 4b) and pervasive schistosity in serpentinite and serpentine schist (Fig. 4c).

Serpentine (antigorite and chrysotile), ilmenite, and rutile are the main rock forming minerals of the wallrock at 1–2.8 m from the fault core and the samples from this part of the host rock profile do not preserve any textural feature of the lherzolite but are turned into a fine-grained dolomitic rocks mostly composed of dolomite, rutile, and ilmenite (Scarsi, 2018; Garofalo et al., 2023).

The contact with the hanging wall damage zone corresponds to the transition from meta-lherzolite to serpentinite and serpentinite schists (e.g., Fig. 2b). Inside the serpentinite, minerals are aligned along a

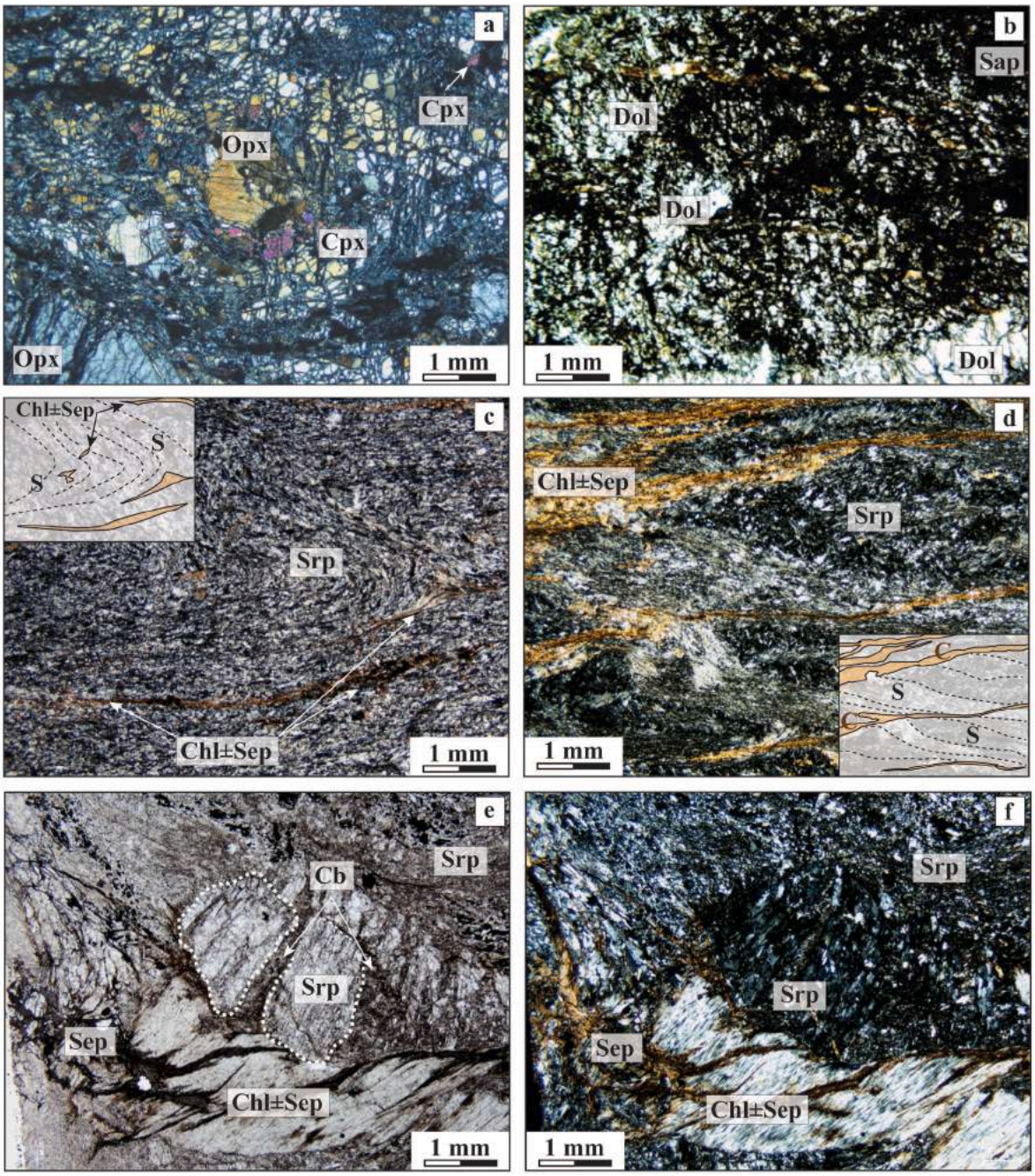

Fig. 4. Photomicrographs of the host rock: (a) Serpentinized lherzolite with ortho- and clinopyroxene crystals replaced by serpentine along the rims. Olivine remnants are also visible, with secondary serpentine veins crosscutting all the previous textures. Cross polarized light microphotograph. (b) Cataclastic sub-angular to well round dolomite grains in a dark felt of saponite. Plane polarized light microphotograph. (c) Serpentinite schist with penetrative, folded foliation made of serpentinite and minor oxides. Brownish patches are composed by late-stage chlorite ± sepiolite felt. Cross polarized light microphotograph. (d) S–C structures developed in serpentinites. "C" shear bands are composed by chlorite ± sepiolite. Cross polarized light microphotograph. (e, f) Serpentinite preserving relics of pyroxene (withe dashed line) undergone to topotactic recrystallization by antigorite and carbonates. Brownish patches are composed by late-stage chlorite ± sepiolite felt and oxides. Plane (e) and cross (f) polarized light microphotograph. Minerals abbreviations (from Whitney and Evans, 2010): Opx, Orthopyroxene; Cpx, Clinopyroxene; Dol: Dolomia; Sap, Saponite; Srp, Serpentine; Chl, Chlorite; Sep, Sepiolite; Cb, Carbonate.

foliation that shows evidence of boudinage (Fig. 4d); also, the newly formed extensional syntaxial carbonate veins (up to 0.2 mm in thickness) are aligned sub-parallel to the foliation. The modal abundance of ilmenite and rutile in this part of the host rock increases considerably.

Approaching the fault core (between ~6.5 and ~3 m from it), the serpentinite develops a mylonitic texture whose microlithons (cf. Passchier and Trouw, 2005) show a top-to-E/NE sense of shear (Fig. 4e and f), in line with the mesoscale observations. Here, the serpentine microlithons are interlayered with domains of authigenic microcrystalline carbonate. Discontinuous quartz-filled veins are also present along

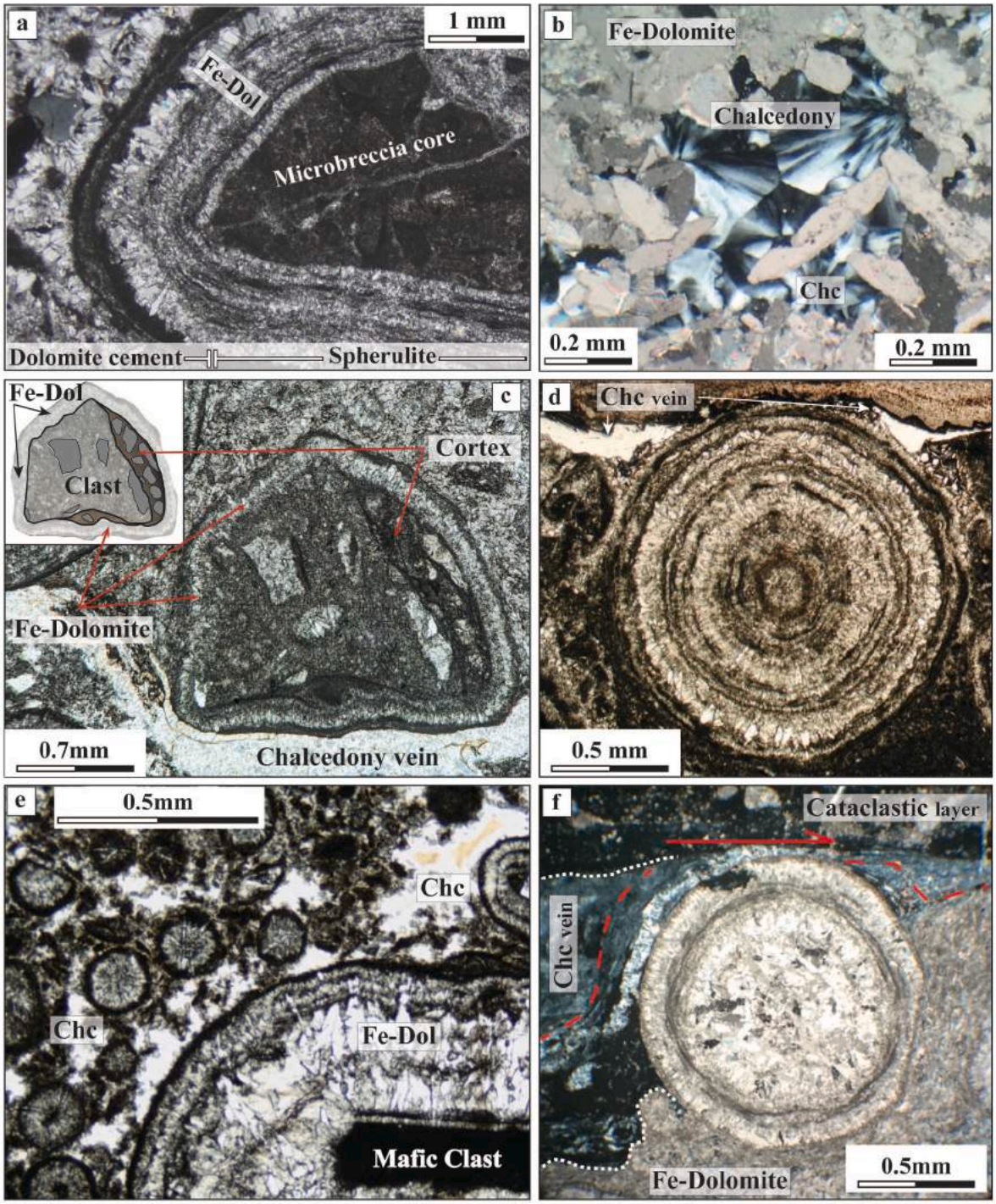

Fig. 5. Photomicrographs of the textures developed inside the spherulite-rich layers. The cements filling the vuggs between single spherulites/clast cortex aggregates are composed by (a) euhedral dolomite (Dol) crystals or (b) chalcedony (Chc, here showing 120° junctions). (c) Clast-cortex aggregate with microbreccia core composed by fragments of carbonates and serpentinite overgrown by concentric Fe-dolomite layer. (d) Spherulite with carbonatic core and several concentric layers (up to 18) made of Fe-dolomite. (e) The size and number of concentric layers is proportional to the size of the spherulites/clast cortex aggregates. The smaller ones are generally massive, while the bigger display several concentric layers, witness of multiple stages of transient growth. Spherulites cores are either composed of serpentinite fragments (dark colored) or carbonates. (f) Example of a spherulite at the contact with a shear vein overgrowth by chalcedony. The red dashed line highlights the dark lamination inside chalcedony, which indicate a dextral sense of shear. (a, c, d, e) plane polarized light microphotographs, (b, f) cross polarized light microphotographs. Minerals abbreviations from Whitney and Evans (2010).

the foliation. In this part of the damage zone, the serpentinite schists show a strong increase in brecciation and progressively turn into a fault gouge. In detail, at a distance of ~1 m from the fault zone contact, is exposed a non-cohesive serpentinite gouge with millimetric, angular to sub-angular serpentine clasts. Here, the clasts still maintain an internal mylonitic foliation with aligned dolomite, rutile, ilmenite and minor pyrite.

At the contact with the fault core, a poorly coherent carbonate level is observed (i.e., the gouge of Fig. 3a). This is a cataclasite made up of very fine-grained, sub-angular to well rounded, randomly oriented dolomite grains enveloped by emerald-green saponite (Fig. 2c and 3a), which forms a dark mantle around the dolomite. This rock, crosscut by randomly oriented dolomite veins (up to 0.3 mm thick), is foliated at the meso-scale (Fig. 2c) but the foliation is no longer evident at the micro-scale (Fig. 3b).

4.2.2. Fault core

Among the structural features at the fault core we recognize (a) layers with dolomitic spherulites and minor clast cortex grains cemented by (ii) chalcedony. Such layers are locally cut by (iii) chalcedony shear veins and, towards the transition between the fault core and the footwall, by (iv) cockade breccias.

In this study the distinction between spherulites and cockade structures (both growing concentric layers formed by radially elongated crystals) was based on the (i) shape and (ii) size of their nucleus. Spherulites always display spherical to subspherical shape and develop around submillimetric nucleus while cockade can be of varied shapes, largely controlled by the geometry of their, millimeter-sized, core clasts.

i) Spherulites-rich layers

Characterised by a porous and vuggy texture (Figs. 2d and 3a-c), these layers are composed by spherulites and (minor) clast-cortex aggregates with euhedral dolomite (e.g., Fig. 5a) and chalcedony (Fig. 5b) filling the volume between single grains.

Spherulites have a subspherical geometry (Figs. 3b–e and 5a, d, e, f), lack of a preferred shape orientation with respect to the shear direction (e.g., Fig. 3a, b, c, e) and nucleate either around submillimetric carbonate nucleus (e.g., Fig. 5d) or submillimetric single grain of the host rock (e.g., relicts of fragments of fault core breccias and relicts of carbonated serpentinite clasts; Fig. 5e) or oxides. Spherulites consistently crystallize as concentric bands of fibrous ferroan dolomite (SEM-EDS spot analyses: CaO, 29.13 ± 2.33 wt%; MgO, 19.03 ± 4.86 wt%; FeO, 1.77 ± 0.87 wt%; Garofalo et al., 2023, Scarsi, 2018) that displays multiple layers of radial crystal growth regularly alternating with darker, oxides-rich concentric bands (Fig. 5d, e, f). These latter are generally thin (up to 0.2 mm) and massive (Fig. 5 a, c, d) but can be locally laminated (Fig. 5e and f). Up to 20 alternating bands were identified in the larger spherulites (Fig. 5d), while are absent in those with diameter <3 mm (Fig. 5e). Concentric growth of spherulites is evident from the microtextural relations between successive bands, which depart radially from the spherulite cores. The growth geometry of acicular ferric dolomite crystals in the spherulites analyzed was quantified using two different types of maps reconstructed from EBSD disorientation data: (i) All-Euler angle maps (Fig. 6a), which are colour-coded images where each colour represents the absolute crystallographic orientation of grains in relation to the SEM reference frame; (ii) Random colour maps, which better highlight individual crystals and their geometries (Fig. 6b and d). These maps confirm that multiple concentric layers of dolomite are formed by acicular crystals radiating out from the centre of the spherulite. Furthermore, schematic representations of crystal models of 8 grains (Fig. 6a) clearly show that all grains are elongated in the direction of one of their a-axes, suggesting that, under the conditions of spherulite formation at Bisciarelle, a is the direction of fastest growth. Grain size ranges from <1 μm to 100 μm, with some of the longer grains measuring 300 μm length and 50 μm width. The disorientation between two grains represents the difference between their crystallographic orientation. This may be best described as the rotation of one crystal relative to the other around a common axis (the disorientation axis). The random pair (i.e. each two grains picked at random in the dataset) disorientation axis distribution was plotted in stereographic projections that use the trigonal symmetry (space group R3) crystallographic reference frame of dolomite (inverse pole figures – IPF) (Fig. 6c and e). Disorientation axes clearly cluster in a girdle contained in the basal plane of dolomite (orthogonal to the c axis), showing that most rotations happen in directions contained in the basal plane and pointing to the centre of the spherulite. This demonstrates that the radial growth of acicular dolomite grains in the concentric layers of spherulites is crystallographically controlled. In addition, close observation of individual grains in the inner and outer concentric layers in Fig. 6 (Fig. 6b and d respectively) confirms that a high number of grains have colour continuity from the inner to the outer layer. This is evidence of epitaxial growth of outer layer crystals as they inherit the orientation of the grain they nucleate upon on the existing spherulite inner layer surface (see also colour continuity in Fig. 6a). This style of crystal growth characterises all concentric dolomite bands observed (Fig. 6).

Clast-cortex grains (Rempe et al., 2014; Rowe and Griffith, 2015; Smith and Faulkner, 2010; Kim et al., 2022) are volumetrically subordinate (<2% of rock volume) and are generally found both at the transition between the spherulites layers and the host-rock or in place with chalcedony shear veins (e.g., Fig. 3e). They have an overall rounded shape, with central clasts made of fragments of the host rock (i.e., serpentinite, ultramafic cataclasite or carbonatic cataclasite) surrounded by a fine-grained outer cortex (Fig. 5c). Clast-cortex grains are in turn surrounded by the rhythmic crystallization of multiple layers of radial ferroan dolomite (Fig. 5c) alternating with darker, oxides-rich concentric bands (likewise spherulites).

ii) Chalcedony cement

The microstructural investigations reveal that in the fault core chalcedony and/or microcrystalline quartz is present in various occurrences, either as filling mineral of empty volumes or as spherical aggregates or as filling mineral of syntectonic veins (chalcedony shear veins).

The chalcedony crystallized within the spherulite-rich layers (e.g., Fig. 5e) shows several textures, namely moss (Fig. 7a), flamboyant (Fig. 7b), wall-lining with central jigsaw texture (Fig. 7c) and fibrous radial (Fig. 7d). All these structures are typical open space filling textures (Moncada et al., 2012, and ref. therein). In place, at the contact with the outer rims of spherulites, chalcedony may occur as spherical aggregates crystallized around the edges of the radial dolomite crystals of the spherulites (Fig. 7e and f). Such spherical arrangement of the cement suggests hetero-epitaxial crystallization of chalcedony on spherulites dolomite crystals (Figs. 6e and 7e, f).

iii) Chalcedony Shear Veins and Injection veins

In places, the chalcedony-bearing shear veins may sharply cut single spherulites (e.g., Fig. 3), but microtextural evidence shows that these veins also grow around spherulites (Fig. 5f). This indicates that spherulite formation and shear deformation were broadly coeval. At the contacts with spherulite-rich layers, these veins are almost entirely made of fine to ultra-fine chalcedony (composition by single-spot SEM-EDS analysis: SiO_2: 97.97 ± 3.23 wt%) locally developing flow banding textures (Fig. 5f).

Millimetric injection-veins, departing from the shear veins, are also observed (Fig. 3c and d). The bulk of these veins is made of angular to sub-angular micro-carbonate clasts (grain size <1.5 mm) interspersed in chalcedony or fine-grained quartz matrix.

The top surface of the chalcedony shear veins is marked by slickenlines (Fig. 3f) and grooves of millimetric to micrometric size (Fig. 7a).

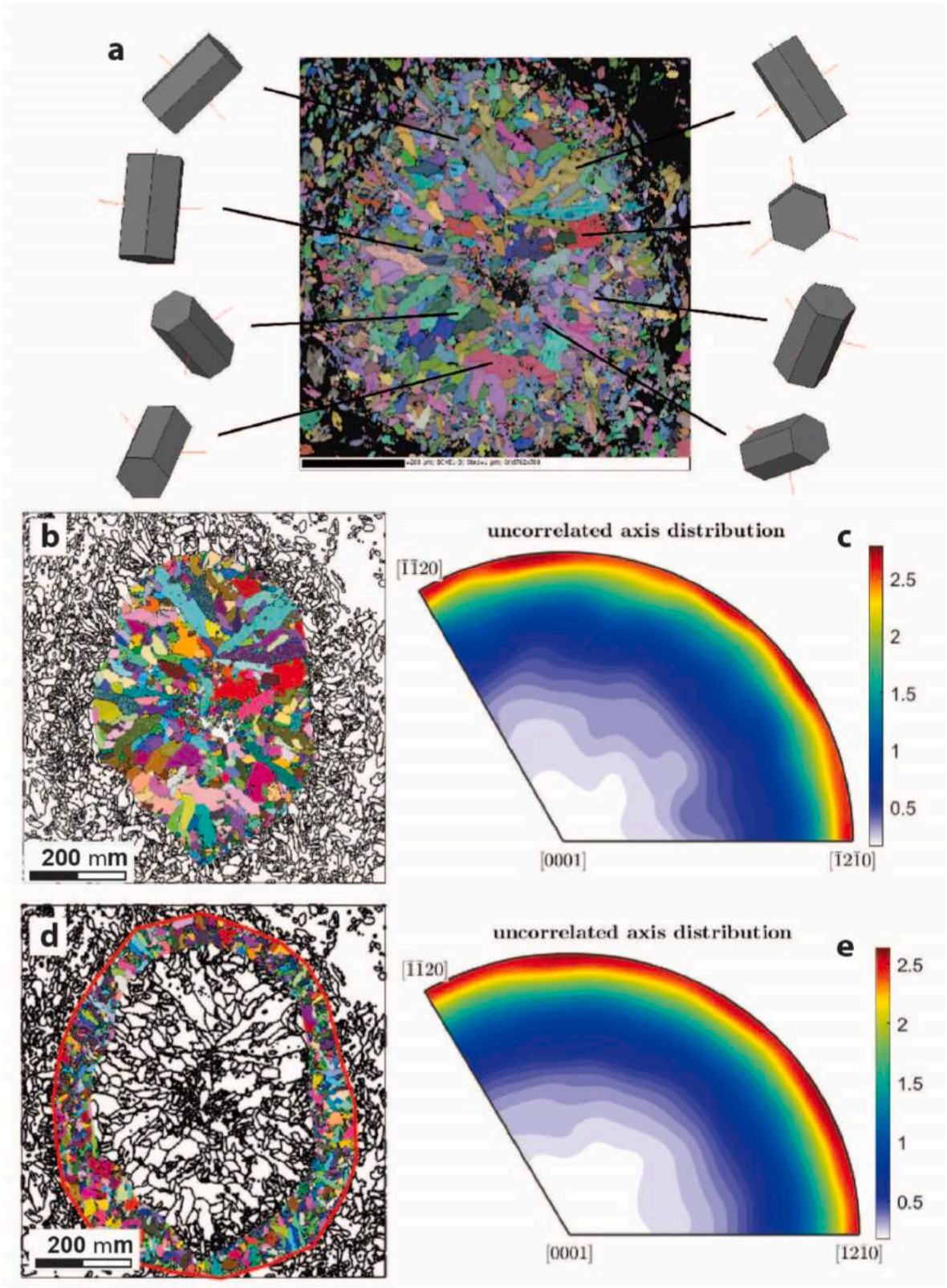

Fig. 6. EBSD analysis of a 400 μm diameter spherulite from the Bisciarelle fault shows concentric layering and a radial structure of dolomite grains. (a) All-Euler angle map where each colour represents an absolute crystallographic orientation. Schematic crystal orientations of 8 grains show that crystals are elongated parallel to one of the a-axes and radiate out from a nucleus in the centre of the spherulite (b) MTEX random colour map of dolomite grains in the spherulite inner layer. (c) Random pair disorientation axis distribution of the inner layer. (d) MTEX colour map of the spherulite outer layer. Grains <50 μm diameter are elongated along directions mostly radiating out, with only some growing tangentially to layering. (e) Random pair disorientation axis distribution of the outer layer showing the same girdle as in (c).

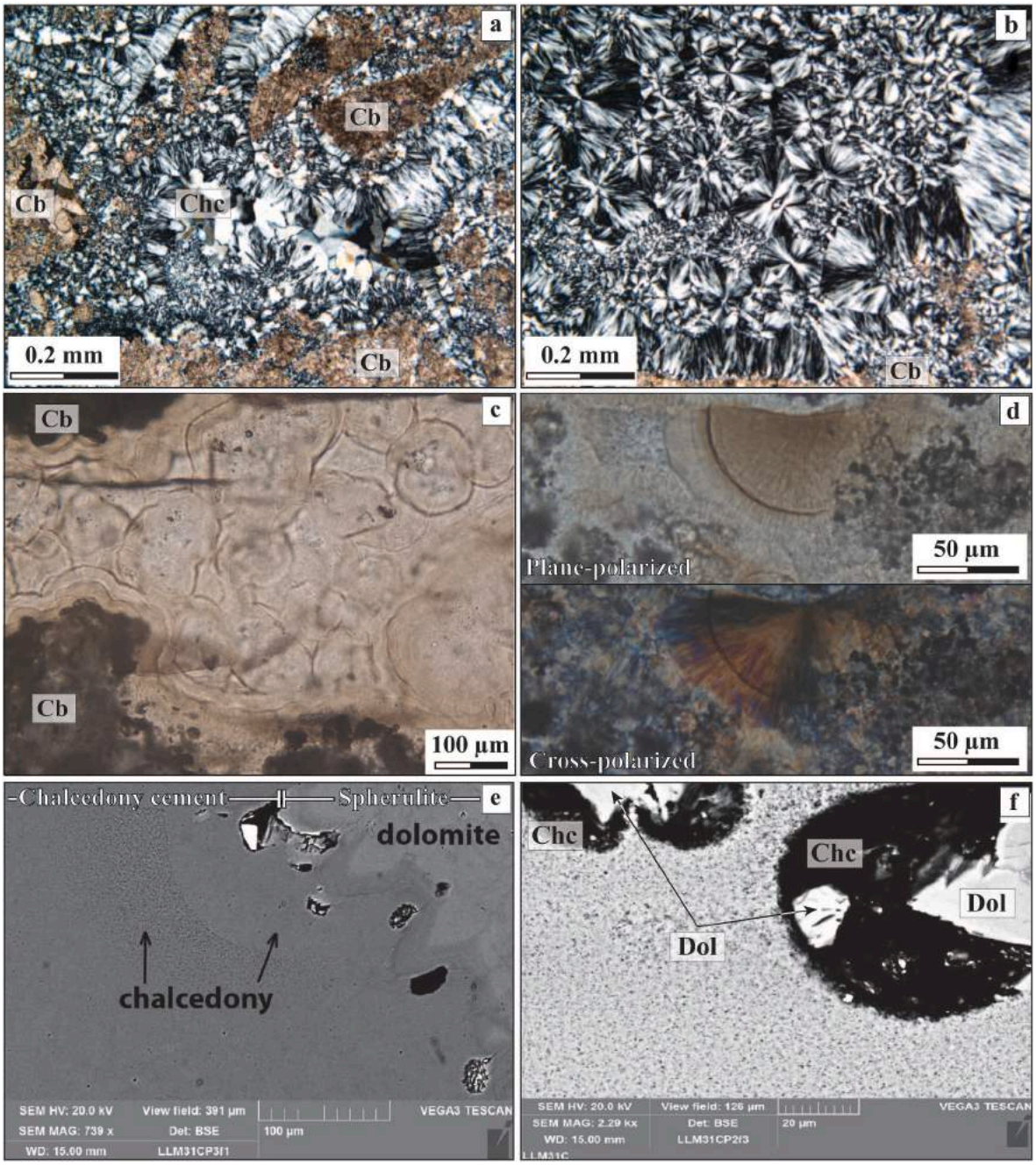

Fig. 7. Photomicrographs of the different chalcedony textures observed inside the vuggs between spherulites and clast cortex aggregates. (a) Chalcedony (Chc) developing moss textures around brownish carbonate fragments (Cb). In the center of the vuggs, chalcedony jigsaw texture can be also recognized. (b) Flamboyant chalcedony textures with minor, brownish carbonate fragments (Cb). (c) Wall lining chalcedony with central jigsaw texture filling vuggs around micrometric carbonate fragments (Cb) (d) Fibrous radial chalcedony. (e) Scanning Electron Microscope (SEM) microphotograph of the contact between a spherulite and the epitaxial chalcedony cement. This latter shows microporosity that sharply decreases at the contact with the dolomite crystals irradiating from the spherulite. (f) Back Scattered Electron (BSE) microphotograph showing the tip of dolomite crystal (Dol) irradiating from a spherulite band in contact with a spherical aggregate of massive chalcedony (Chc) containing dolomite fragments. (a, b) cross polarized light microphotographs, (c) plane polarized light microphotographs. Minerals abbreviations from Whitney and Evans (2010).

These slip surfaces show the presence of <1 µm euhedral quartz crystals surrounded by a fibrous silica matrix (Fig. 7b), which is similar to the glass filaments produced in experiments of quartz sand deformation at high slip velocities (Hayward et al., 2016). In places, the outer surfaces of spherulite grains are sites of strain concentration and show micron-sized slickenlines and grooves (Fig. 7c). These are coated by sub-micron carbonate grains (from 200 nm to 1 µm in diameter; Fig. 7d), similar to those found in mirror-like surfaces for which a genesis by shear localization during high velocity slips was documented (Rowe and Griffith, 2015, and ref. therein).

iv) Cockade breccia

Cockade breccia (cf. Berger and Herwegh, 2019; Genna et al., 1996) differ from the spherulites layers for the bigger clast size (cm in size), the shape (generally angular to sub-angular) of core clasts (cm in size) and the interstitial cement (made of carbonate). Concentric bands of carbonate grains grow with crystals radially arranged around serpentinite

and carbonated serpentinite clasts.

5. Discussion

In the complex tectonic evolution of the Voltri Massif, the Bisciarelle fault zone preserves evidence of late stage brittle deformation, in particular during the top-to-NE and the top-to-E tectonic transport phase of late Oligocene/early Miocene age (Capponi and Crispini, 2002; Federico et al., 2009, 2014; Spagnolo et al., 2007). The preserved brittle structures (e.g., fragmented spherulites, clast-cortex aggregates, cockade breccias and multiple-stages vein sets) were likely developed at shallow crustal condition (e.g., 7.5–15 MPa and 250–300 °C), as suggested by the P-T entrapment conditions estimated for the H_2O–CO_2 fluid inclusions found in the ore veins of the Lavagnina Lakes (Giorza, 2010).

The petrographic and microstructural datasets presented here provide additional insights into the controls of metasomatic fluids on fault rupture processes.

5.1. Syntectonic fluid-rock interaction in the damage zone

In fault zones the permeability is high in the damage zone and becomes dynamically lower inside the fine-grained, highly-comminuted fault core (e.g., Billi et al., 2003). Because damage zones develop early in a fault's history, and because fault cores can nucleate from damage zones (Choi et al., 2016; Kim et al., 2004), fluid-fault interaction is expected to be more intense in the damage zones since the inception of faulting (e.g., Faulkner et al., 2010 and references therein). Inside the Bisciarelle fault zone, the asymmetric hanging wall and footwall damage zones (Fig. 2b and c) develop typical second-order structures (Choi et al., 2016), with calcite and/or serpentine veins and boudinage coupled with pervasive metasomatic alteration halos (Fig. 2a and b). Here, the interaction of the protolith with hydrothermal fluids substantially modifies the fault rocks petrography (e.g., Garofalo et al., 2023; Scarsi, 2018; Giorza, 2010) and, likely, the rheological properties of the bulk host rock. Geochemical analyses (see Garofalo et al., 2023; Scarsi, 2018 for details) of the hanging wall damage zone (typically serpentinized lherzolite of the Erro-Tobbio unit) show that, while a large number of chemical components were mobile at the time of faulting, only volatiles (mainly H_2O and CO_2) and a limited number of components (Si, Ca, Sb, W) were systematically gained by the rock as a result of diffusion (metasomatic reactions) and mass addition due to advection (veining). These components were likely transported by the fluid during coseismic events and periods of enhanced permeability, and then precipitated in the wall-rock veins early in the faulting cycle. Enhanced porosity within the fault core promoted fluid channelling under overpressure condition (e.g., Blanpied et al., 1992; Rice, 1992; Speckbacher et al., 2012; Locatelli et al., 2018, 2019), which represents an effective weakening mechanism (e.g., Wang et al., 2014; Speckbacher et al., 2011). This process is evidenced by the cyclic and localized growth of calcedony-rich veins, cockade breccias, spherulites and clast-cortex aggregates. Their occurrence only inside the fault core of the Bisciarelle fault system suggest that they were the products of successive events of shear deformation supported by localized, vigorous fluid flow. Another feedback of fluid channelling was the resulting mass gains – due to serpentinization and carbonation (Scarsi, 2018; Garofalo et al., 2023) – that progressively modified the mineral composition of the fault rock. The crystallization of newly formed weak minerals (e.g., saponite, serpentine and chalcedony; Rutter et al., 1986; Moore and Rymer, 2007; Speckbacher et al., 2012) significantly weakened the fault zone (e.g., Wang et al., 2014) and promoted localized shear deformation (e.g., along chalcedony slip surfaces; Fig. 3c–f, g). This is substantially different from other upper-crustal fault zones in peridotite, where comminution by cataclasis under fluid poor conditions is the dominant process.

5.2. Dolomitic spherulites

Textural and structural data such as (i) the occurrence of ferroan dolomite spherulite-rich layers at the core of the Bisciarelle fault zone, (ii) the close packing between the spherulites (iii) the high porosity of the fault matrix with round shaped, rhythmically concentric spherulite texture and (iv) the occurrence of clast-cortex aggregates and cockades breccia layers suggest that the core of the fault nucleated as hybrid fracture (i.e., with transient switch from extension to shear fracture; Ramsey and Chester, 2004). This process, characterized by synchronous fracture opening and sliding, combined with increase in rock volume (Fossen, 2016), was cyclic, as testified by the concentric banded texture of the spherulites (Figs. 3e and 5a, c, d, e, f). Also, the supersaturated fluid influx associated with faulting is likely to have led to fast mineral precipitation, as evidenced by the delicate acicular texture of ferroan dolomite constituting the bulk of the spherulites. Their radial growth (EBSD data in Fig. 6) testifies the lack of any preferential orientation with respect to the fault walls (i.e., no iso-orientation respect to the top-to-NE main sense of shear; Fig. 2a and b) suggesting fast and cyclic mineral precipitation events in a fluid. These would require sudden fluid pressure drops of highly supersaturated fluids. This is also in agreement with the radial crystal textures developed in cockades breccia layers, attributed by Berger and Herwegh (2019) to fast fluid precipitation events triggered by seismic event.

The evidence for (i) spherulite brecciation, with also brecciated rock fragments at the core of single spherulites/clast cortex aggregates (Fig. 3e and 5c), and (ii) chalcedony shear veins crosscutting mixed spherulite and cockade breccia layers (Fig. 3a-c, e, f) point to a growth mechanism whereby episodes of spherulite nucleation and growth were alternated with episodes of localised shear deformation and brecciation. Nevertheless, the spherical shapes of spherulites (e.g., Fig 2d and 3b), the crystallization of spherical aggregates in the chalcedony cement (Fig. 7e and f) and the high volume of cement vs spherulites/clasts testify the persistence of high-permeability, fluid-dominated conditions (e.g., Banala et al., 2019) at the fault core. Also, the occurrence of multiple events of cockade cement precipitation (i.e., in the cockade breccia layers, Fig. 3e) testify that deformation processes were mediated by fluid-dominated conditions.

The mechanism of spherulite growth within the fault core is an interesting aspect of this faulting process at shallow depths. Spherulite growth is interpreted in previous studies as a fast, non-equilibrium process that leads to polycrystalline growth due to quenching of highly supersaturated fluids (Beck and Andreassen, 2010; Gránásy et al., 2005; Rodriguez-Blanco et al., 2017). Spherulitic growth proceeds via nucleation of new particles onto existing cores ("growth front nucleation", cf. Gránásy et al., 2005) or via non-crystallographic branching (e.g., Nakamuro et al., 2021) and may also involve additions of nanoparticles via a process known as Oswald ripening (e.g., Rodriguez--Blanco et al., 2017). The highly rounded spherulites of Bisciarelle display concentric growth bands with densely branching radial crystal structures (Fig. 5a–c, d, e, f) and are likely to belong to the "sphere" category (Fig. 5.3e in Rodriguez-Blanco et al., 2017), for which fast crystallization under conditions of extremely-high fluid supersaturation is experimentally proven (Andreassen et al., 2010). Under these conditions, each of the Bisciarelle spherulite layers likely crystallized by quenching of highly supersaturated fluids which carried high concentrations of CO_2 and Fe, as well as Ca, Mg, Si, Sb, and W (Garofalo et al., 2023). Fluid flow probably also triggered the phase separation (effervescence) of a CO_2-rich vapour phase from a H_2O-rich liquid phase (Duan et al., 1995; Hu et al., 2007) and the high content of vapour phase fostered epitaxial growth (Sunagawa, 1978) within the spherulites between radial crystals across concentric growth bands (e.g., Fig. 5d, e, and 6). Rapid nucleation and precipitation events were eventually interspersed with transient fluid pressure drops and progressive strain accumulation by cataclastic flow (i.e., rolling, sliding, and fracturing; Fig. 3e and 5c) of newly formed spherulites, a process comparable to

that experimentally reproduced by Kim et al. (2022). These cycles were repeated several times before the final sealing of the fault core, as suggested by the multiple alternating bands observed in larger spherulites (e.g., Fig. 3e and 5d).

The hypothesis of a H_2O–CO_2 fluid circulating within the fault core is strengthened by the study of Giorza (2010), who documented H_2O–CO_2 fluid inclusions (X_{CO2}: 0.02–0.03) inside ferroan dolomite. Thus, in the Bisciarelle fault zone, a CO_2-rich hydrothermal fluid mediated the fault's activity by generating the metasomatic assemblage of the damage zone, the associated veins, and the peculiar fault core rocks observed.

5.3. Conceptual model of the fault zone evolution

We propose a conceptual model for the structural evolution of the Bisciarelle fault zone that integrates field, microstructural, and analytical data (Fig. 9).

The finite strain of the fault was mediated by cycles of fluid pressure build-ups, fault opening, fluid flow, and mineral precipitation during seismic failure similar to the fluid-activated fault valve model of Sibson et al. (1988). After the generation of the damage zone, we propose four stages of fault core formation and stick-slip fault motion. At stage T1 (Fig. 9), fault core nucleation resulted from transiently elevated P_{fluid}, which promoted weakening and hybrid dilation and fracturing. Interestingly, the location of the newly opened fault segment observed in the field, is asymmetric with respect to the fault architecture (Fig. 2a), similar to what has typically been documented for master faults (Billi et al., 2003). At this stage the fluid/rock ratio increases along the fault, enhancing the width of the metasomatic front.

The opening to metasomatic fluid circulation led to co-seismic slip due to the weakening caused by fluid over-pressure (stage T2a) generating the hydraulic breccia found in the footwall damage zone (Fig. 2c). Pulverization of clasts provided the fragments that acted as nucleation sites (e.g., Fig. 5e) for the next cycle of spherulite growth (stage T2b). Such rapid and extensive nucleation of ferroan dolomite spherulites was supported by transient flow of highly supersaturated metasomatic fluids within the fault core. The crystallization of spherulites, with concentric growth bands and dense radial crystal structures, via "growth front nucleation" was promoted by rapid fluid pressure drops (T2b, Fig. 9), which in turn promoted ferroan dolomite precipitation from the highly supersaturated CO_2-rich hydrothermal fluids. Little or no silica precipitation is observed at this stage, probably due to a relatively high fluid pH that held silica in solution (Fournier, 1985). During the inter-seismic

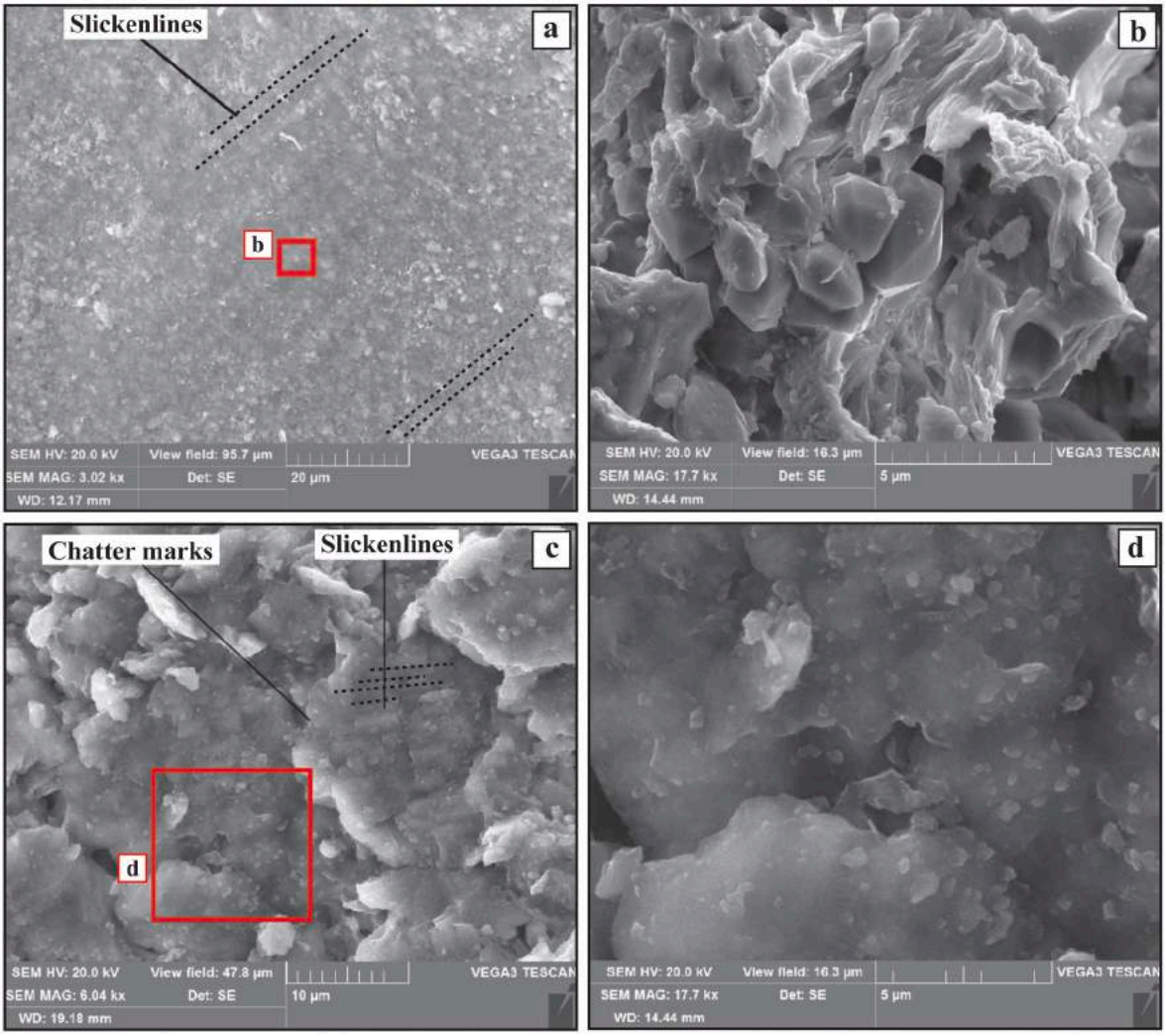

Fig. 8. Scanning Electron Microscope (SEM) microphotographs of the textures developed in spherulites and chalcedony shear veins. (a) Slip surface developed along a chalcedony shear vein marked by micrometric slickenlines (black dashed lines). (b) Magnification of the previous slip surfaces, composed by < 1 µm euhedral quartz crystals surrounded by a fibrous silica matrix. (c) Carbonate slip surface marked by micrometric chatter marks and slickenlines (black dashed lines) developed on the outermost of the concentric layers of a spherulite. (d) Magnification of the previous slip surfaces, composed by micrometric to sub-micrometric carbonate grains coating.

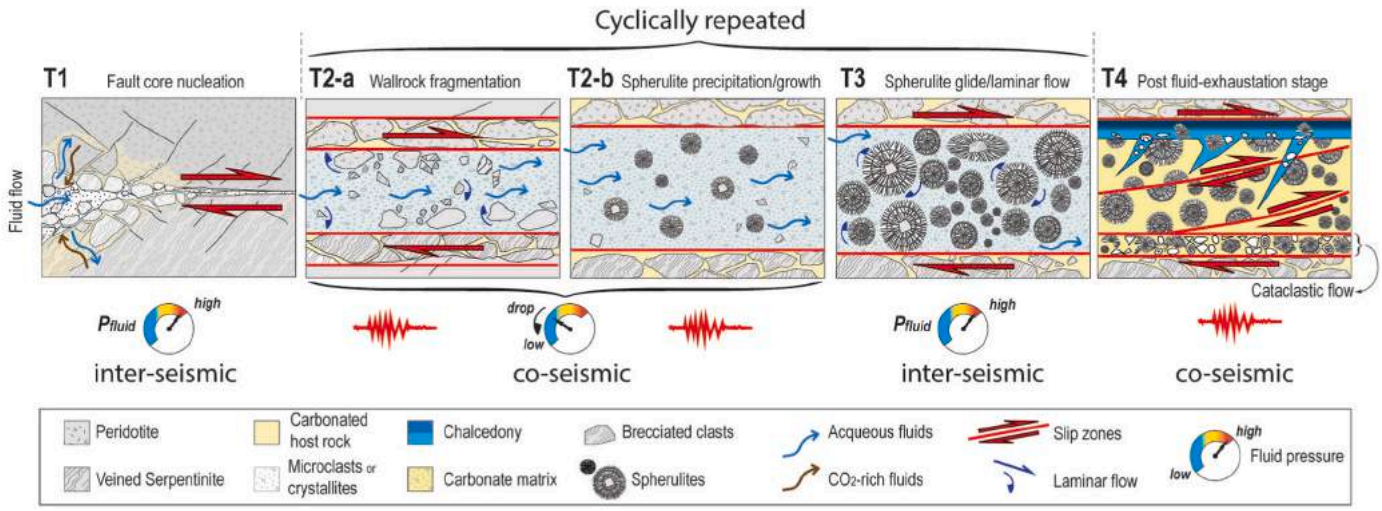

Fig. 9. Conceptual model of the structural evolution of the Bisciarelle fault zone (see text for the explanation).

stage of fluid pressure build up (stage T3) spherulite growth was inhibited. Individual spherulites were probably floating within the fault fluid in a way that is comparable to that described for fluidization of fault damage zones (Cox and Munroe, 2016) and aligned (Fig. 3b–e) sub-parallel to the flow lines during laminar flow (Rowe and Griffith, 2015). T2a, T2b and T3 stages, with transient P_{fluid} increases and drops, were repeated cyclically during the stick-slip motion of the fault and each cycle corresponds to one or more sets of concentric bands recorded in the largest spherulites. Upon the exhaustion of available hydrothermal fluids, no further spherulite bands or silica matrix developed, the fault sealed and strengthened. This generated a rheological contrast between the spherulites-rich fault core and the neighboring fault gouge (Figs. 2b and 3a); thus, faulting proceeded via different processes.

This last stage of fault activity (stage T4) was likely co-seismic and caused by transient (and renewed) increase of P_{fluid}. This stage was characterized by development of mirror-like slip surfaces (e.g., Fig. 3e) and injection veins irradiating from newly formed chalcedony shear veins (e.g., Fig. 3c and d), which intersected the spherulites microbreccia layers nucleated at, or close to, the transition zone of the fault. The rapid fault slip induced a sudden fluid pressure drop in the fault, which in turn caused flashing and phase separation. During this last stage of faulting, chalcedony and quartz precipitated. Microstructural evidence for chalcedony and quartz forming open-space filling textures (Fig. 7a–f) are consistent with crystallization via phase-separation processes (Moncada et al., 2012) of immiscible CO_2–H_2O fluids (Kaszuba et al., 2006). The formation of amorphous silica in the fault led to a dramatic loss of strength along the slip surfaces (Faber et al., 2014), localising the deformation and thus preventing the spherulites layers from experiencing further intense deformation during this stage.

5.4. Evidence for paleo-seismic activity and regional implications

We propose that recognition of repeated fluid pulses (supporting spherulites growth) and repeated instances of brittle deformation (with characteristic textures) may be used as indicators of seismicity in the Bisciarelle rock record.

The finding of a unique rock record indicative of seismic activity is still largely debated, and multiple examples are proposed by several authors (e.g., Sibson, 1986; Rowe and Griffith, 2015; Cowan, 1999; Hayward et al., 2016; Berger and Herwegh, 2019). Taking into account this debate, here we report several structural observations that suggest paleo-seismic activity along the Bisciarele Fault zone. Moving from the inner structures developed at the fault core to those observed in the damage zone:

(i) At the fault core, the concentric textures of bigger spherulites are evidence of fast and cyclic mineral precipitation events. Such process would require a supersaturated fluid (e.g., in CO_2) experiencing transient and rapid P_{fluid} drops, conditions that may be achieved during a co-seismic event in a fluid-saturated fault zone (e.g., Broadwell et al., 2019).

(ii) Clast cortex aggregates (e.g., Fig. 5c and d) found at the transition fault core-damage zone are comparable to those obtained by experiments at seismic and sub-seismic slip rates (Kim et al., 2022) with both natural and laboratory-produced clast cortex aggregates consisting of nanocrystals (nanoparticles) produced by episodic cataclasis, wear, and amorphization.

(iii) On the slickenlines and chatter marks of the mirror-like surfaces cutting the Bisciarelle spherulites, sub-micrometric, euhedral carbonate crystals are generally found (e.g., Fig. 7c and d). These latter are an analogue of those observed on the mirror-like surfaces resulting by extreme shear localization during high velocity slips (both in natural and laboratory samples; Rowe and Griffith, 2015, and ref. therein).

(iv) Within the spherulite layers the chalcedony infilling the voids develop moss and flamboyant textures (Fig. 8a and b). These result from the precipitation of colloidal amorphous silica (Moncada et al., 2012), a lubricating media similar to the silica gels formed both in natural faults and in rock friction experiment, possibly linked to a mechanism of coseismic weakening (Kirkpatrick et al., 2013).

(v) On the slip surfaces of chalcedony veins, slickenlines are associated to filamentous amorphous silica (Fig. 7a and b), this texture is similar to that of the glass filament generated at high-velocity ($V > 10$ cms^{-1}) during slip experiments (Hayward et al., 2016).

(vi) At the transition between fault core and hangingwall damage zone, spherulite layers are intersected by wedge-shaped injection veins departing from a late-stage chalcedony shear vein (Fig. 3c and d). Their dimensions, morphology, and layer dip angles are comparable to the off-fault tensile fractures reported both on seismogenic faults and experimental settings (Rowe and Griffith, 2015).

(vii) At the transition fault core-footwall damage zone, the spherulite layers are bounded by cockade breccias (Fig. 3f and g) These have been interpreted to represent field evidence of sustained high fluid flux and fast mineral precipitation (e.g. Cox and Munroe, 2016; Masoch et al., 2019). Berger and Herwegh (2019) attributed each concentric layer of radial crystal growth in cockades to a fluid influx event, in turn triggered by a seismic event.

Therefore, multiple concentric layers represent cycles of fluid influx and seismic activity.

The recognition of seismic events ascribed to the late Oligocene-early Miocene is a novelty in the context of the Ligurian Alps. Only recently (Mueller et al., 2023) recognized evidence of syn-depositional seismicity in mixed carbonate-siliciclastic sediments of Langhian-Serravallian times of the Finale Ligure Basin (Western Liguria). The late Oligocene-early Miocene interval is characterized in the Ligurian Alps geodynamic framework by the inception of the Ligurian-Provençal back-arc basin opening (~35-30 Ma), the counterclockwise rotation of the Corsica-Sardinia block and the eastward retreat of the Apenninic slab (e.g. Laubscher et al., 1992; Vanossi et al., 1994; Rollet et al., 2002; Morelli et al., 2022). This rotation has probably been accommodated by a mega strike-slip zone (Federico et al., 2009, 2014; Maino et al., 2013) that locally showed transtensional (see Mueller et al., 2023) or transpressional character, with associated reverse faults (Spagnolo et al., 2007; Crispini et al., 2009). In this context, the Bisciarelle fault system would represent the seismic remnants of this complex, long-lived geodynamic event. Further research will be necessary to better constrain the P-T conditions of Bisciarelle fault system formation and its significance within the regional tectonic framework, only partly understood.

6. Conclusions

By combining field and multi-technique analytical data, we show that the complex structural evolution of a fluid-rich fault zone hosted by ultramafic wallrocks can be efficiently unravelled, including the possible relations with cycles of paleo-seismic events.

A first important result of our study is the recognition of concomitant wallrock metasomatism and faulting processes in an upper crustal fault damage zone and fault core. This results in a coherent set of information regarding the chemical and mineralogical modification of the wallrock, the structural evolution of the fault, and the formation of syn-kinematic mineralizations. Most probably, wallrock hydration due to serpentinization and carbonation of the Bisciarelle ultramafic rocks modified radically the compositions of the wallrock and caused fault weakening and localization of successive shear events. The serpentinites and the dolomitic fault core could have formed a bi-material interface, which changed irreversibly the mechanical behaviour of the wallrocks. In particular, the shear surfaces could have developed as seismic ruptures within the serpentinites.

The mechanism of spherulite growth within the fault core is probably the most intriguing process that occurred during faulting at Bisciarelle. We propose fast spherulite growth via front nucleation processes, which involves a CO_2-rich, phase-separating (i.e., effervescing) hydrothermal fluid: this implies a close association between spherulites and co-seismic structures and supports the hypothesis that they are syn-kinematic. For this reason, our conceptual model of structural evolution of the fault zone combines spherulite genesis with formation of the documented meso- and microstructures (recrystallization textures chalcedony shear veins, filamentous silica, mirror-like slip surfaces, etc.), which suggest cumulative seismic ruptures. This interpretation of spherulites reconciles with – quite surprisingly – the growth of undeformed, delicate structures and deformation at seismic velocities. The so far scarce documentation of spherulites in field studies of fault zones suggests either that they are rare, or alternatively that they have been so far overlooked.

CRediT authorship contribution statement

Michele Locatelli: Data curation, Formal analysis, Funding acquisition, Methodology, Validation, Writing – review & editing. **Laura Crispini:** Conceptualization, Data curation, Funding acquisition, Investigation, Methodology, Supervision, Writing – original draft, Writing – review & editing. **Elisabetta Mariani:** Data curation, Investigation, Methodology, Validation, Writing – original draft, Writing – review & editing. **Giovanni Capponi:** Conceptualization, Investigation, Writing – original draft, Writing – review & editing. **Marco Scarsi:** Formal analysis, Investigation, Writing – original draft. **Laura Federico:** Data curation, Funding acquisition, Investigation, Methodology, Validation, Writing – original draft, Writing – review & editing.

Declaration of competing interest

The authors declare that they have no known competing financial interests or personal relationships that could have appeared to influence the work reported in this paper.

Data availability

Data will be made available on request.

Acknowledgements

The Authors wish to thank Matteo Maino and an unknown reviewer for their constructive revision that helped to improve the manuscript. The Authors wish to thank also Eugenio Fazio for the careful editorial handling of the paper during the review process. EM acknowledges the EBSD-SEM Laboratory, now part of the SEM SRF at the University of Liverpool, for supporting all EBSD analyses. ML thanks the University of Genoa for the publication of this paper ((grant no. 100022-2023-ML-FRA_001). LC and LF thank the PRIN-MUR (Italian Research Projects of Relevant National Interest, funding no. 2020542ET7_002). ML is part of the Italian PNRR-RETURN project.

Appendix

Geochemistry of Bisciarelle fluids

A detailed discussion on the mechanism(s) that controlled transport and precipitation of Au and the suite of trace elements within the fault fluid goes beyond the scope of this work; however, we stress the similarities between the geological setting of Bisciarelle and that of the typical orogenic, vein-hosted Au deposits, as well as the similarities between the physical-chemical properties of the Bisciarelle fluid and those of the orogenic Au fluids (Fusswinkel et al., 2017; Garofalo et al., 2014, Garofalo et al., 2023). If this hypothesis is true, then the source region of the Bisciarelle fluid must be located at depths where metamorphic dehydration of the Voltri crust occurred, and/or in sections of the crust in which magmatic-hydrothermal fluids were produced (cf. Ridley and Diamond, 2000). An indirect clue of fluid source is given by the crust-normalized composition of the dolomitic spherulites (Fig. A1), which shows evidence for mass fractions of Ca and other metals (Mg, Sr, Ni, not shown) having a crustal signature, but mass fractions of REEs being extremely depleted with respect to the upper continental crust. The flat patterns of Fig. A1 indicate, in general, a composition of the fault fluid that did not change significantly its metal budget during spherulite formation. The REE depletions might be the effect of a fluid that deposited much of its REE budget within the fault before forming the spherulites, and/or those of a fault fluid that was inherently REE-poor and did not experience significant chemical interaction with the crust. More details can be found in Scarsi (2018); Garofalo et al. (2023).

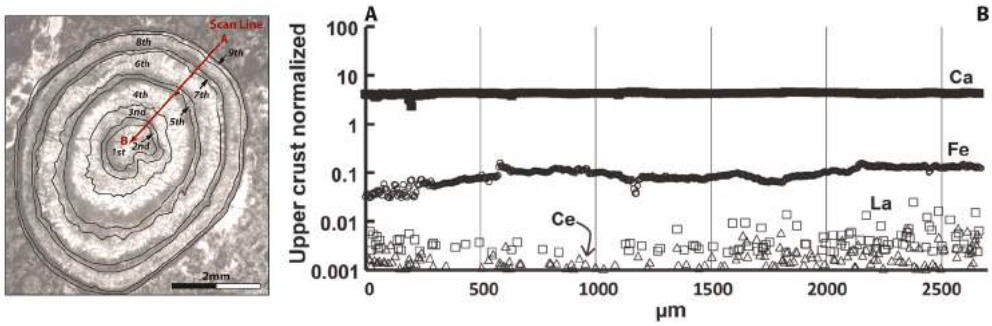

Fig. A1. Concentrations of a representative set of spherulite components analyzed by line scan LA-ICP-TOFMS analyses and normalized with respect to the upper crust (upper crust data: Rudnick and Gao, 2003). Line scan direction over the spherulite concentric layers is shown by the red arrow. Plane polarized light microphotographs of spherulite was modified from Scarsi (2018).

Do Spherulite have sedimentary origin?

The most characteristic features found in the fault core are the dolomitic spherulites, which macroscopic morphology resembles pisolite or cave pearls (e.g., Nader, 2007), usually thought to be related to vadose groundwater circulation or to oolite/pisolite deposits related to hydrothermal circulation (e.g., Sant'Anna et al., 2004; Wu et al., 2014).

Nevertheless, pieces of evidence suggest that the studied dolomitic spherulites could not result from the brittle reworking of a previous, pisolite-bearing sedimentary limestone. At first, any brittle deformation of a pristine limestone would have caused pervasive cataclasis and grain size reduction. These textures are simply missing in the Bisciarelle fault rocks, which are instead characterized by high roundness and circularity of the spherulites (Figs. 3a-c, e and 5d, e, f), stages of undisturbed epitaxial growth, and porous and open-space-filling textures (Figs. 5a, b, e and 7a-d). Another argument against a pre-existing limestone at the core of the fault is geochemical – the flow of a H_2O–CO_2, metal-rich hydrothermal fluid metasomatizing the host meta-lherzolite is inconsistent with the passive role of a reworked limestone within the fault.

References

Andreassen, J.-P., Flaten, E.M., Beck, R., Lewis, A.E., 2010. Investigations of spherulitic growth in industrial crystallization. Chem. Eng. Res. Des. 88, 1163–1168.

Bachmann, F., Hielscher, R., Schaeben, H., 2010. Texture analysis with MTEX–free and open source software toolbox. Solid State Phenom. 160, 63–68.

Banala, A., Ma, H., Kumar, A., 2019. Influence of particulate geometry on permeability of porous materials. Powder Technol. 345, 704–716.

Beck, R., Andreassen, J.-P., 2010. The onset of spherulitic growth in crystallization of calcium carbonate. J. Cryst. Growth 312, 2226–2238.

Berger, A., Herwegh, M., 2019. Cockade structures as a paleo-earthquake proxy in upper crustal hydrothermal systems. Sci. Rep. 9 (1), 9209.

Belogub, E.V., Melekestseva, I.Y., Novoselov, K.A., Zabotina, M.V., Tret'yakov, G.A., Zaykov, V.V., Yuminov, A.M., 2017. Listvenite-related gold deposits of the South Urals (Russia): a review. Ore Geol. Rev. 85, 247–270.

Billi, A., Salvini, F., Storti, F., 2003. The damage zone-fault core transition in carbonate rocks: implications for fault growth, structure and permeability. J. Struct. Geol. 25, 1779–1794.

Blanpied, M.L., Lockner, D.A., Byerlee, J.D., 1992. An earthquake mechanism based on rapid sealing of faults. Nature 358, 574–576. https://doi.org/10.1038/358574a0.

Broadwell, K.S., Locatelli, M., Verlaguet, A., Agard, P., Caddick, M.J., 2019. Transient and periodic brittle deformation of eclogites during intermediate-depth subduction. Earth Planet Sci. Lett. 521, 91–102.

Brodsky, E.E., Kanamori, H., 2001. Elastohydrodynamic lubrication of faults. J. Geophys. Res. Solid Earth 106, 16357–16374.

Caine, J.S., Forster, C.B., 2013. Fault zone architecture and fluid flow: insights from field data and numerical modeling. In: Haneberg, W., Mozley, P., Moore, J., Goodwin, L. (Eds.), Faults and Subsurface Fluid Flow in the Shallow Crust.

Cannaò, E., Scambelluri, M., Agostini, S., Tonarini, S., Godard, M., 2016. Linking serpentinite geochemistry with tectonic evolution at the subduction plate-interface: the Voltri Massif case study (Ligurian Western Alps, Italy). Geochem. Cosmochim. Acta 190, 115–133.

Capponi, G., Crispini, L., 1997. Progressive shear deformation in the metasediments of the Voltri Group (Ligurian Alps, Italy); occurrence of structures recording extension parallel to the regional foliation. Boll. Soc. Geol. Ital. 116, 267–277.

Capponi, G., Crispini, L., 2002. Structural and metamorphic signature of alpine tectonics in the Voltri Massif (Ligurian Alps, North-Western Italy). Eclogae Geol. Helv. 95, 31–42.

Capponi, G., Crispini, L., Federico, L., Malatesta, C., 2016. Ital. J. Geosci 135 (1), 157–169. https://doi.org/10.3301/IJG.2015.06.

Capponi, G., Crispini, L., Ferrarazzo, I., 1998. New field data on the case ferrere area (Voltri Massif, Ligurian Alps). Boll. Soc. Geol. Ital. 117, 87–92.

Cathles, L.M., 1991. The importance of vein selvaging in controlling the intensity and character of subsurface alteration in hydrothermal systems. Econ. Geol. 86, 466–471.

Choi, J.-H., Edwards, P., Ko, K., Kim, Y.-S., 2016. Definition and classification of fault damage zones: a review and a new methodological approach. Earth Sci. Rev. 152, 70–87.

Cimmino, F., Messiga, B., 1979. I calcescisti del Gruppo di Voltri (Liguria Occidentale): le variazioni composizionali delle miche bianche in rapporto alla evoluzione tettonico-metamorfica alpina. Ofioliti 4, 269–294.

Cox, S.F., Munroe, S.M., 2016. Breccia formation by particle fluidization in fault zones: implications for transitory, rupture-controlled fluid flow regimes in hydrothermal systems. Am. J. Sci. https://doi.org/10.2475/03.2016.02.

Cowan, D.S., 1999. Do faults preserve a record of seismic slip? A field geologist's opinion. J. Struct. Geol. 8 (21), 995–1001.

Crispini, L., Federico, L., Capponi, G., Spagnolo, C., 2009. Late orogenic transpressional tectonics in the «Ligurian Knot. Boll. Soc. Geol. Ital. 128 (2), 433–441.

Desmons, J., Aprahamian, J., Compagnoni, R., Cortesogno, L., Frey, M., 1999. Alpine metamorphism of the Western Alps: I. Middle to high T/P metamorphism. Schweizerische Mineralogische und Petrographische Mitteilungen 79, 89–110.

Di Toro, G., Han, R., Hirose, T., De Paola, N., Nielsen, S., Mizoguchi, K., Ferri, F., Cocco, M., Shimamoto, T., 2011. Fault lubrication during earthquakes. Nature 471, 494–498.

Di Toro, G., Hirose, T., Nielsen, S., Pennacchioni, G., Shimamoto, T., 2006. Natural and experimental evidence of melt lubrication of faults during earthquakes. Science 311, 647–649.

Duan, Z., Moller, N., Weare, J.H., 1995. Equation of state for the NaCl-H2O-CO2 system: prediction of phase equilibria and volumetric properties. Geochem. Cosmochim. Acta 59, 2869–2882.

Evans, J.P., Prante, M.R., Janecke, S.U., Ault, A.K., Newell, D.L., 2014. Hot faults: iridescent slip surfaces with metallic luster document high-temperature ancient seismicity in the Wasatch fault zone, Utah, USA. Geology 42, 623–626.

Faber, C., Rowe, C.D., Miller, J.A., Fagereng, Å., Neethling, J.H., 2014. Silica gel in a fault slip surface: field evidence for palaeo-earthquakes? J. Struct. Geol. 69, 108–121.

Faulkner, D.R., Jackson, C.A.L., Lunn, R.J., Schlische, R.W., Shipton, Z.K., Wibberley, C. A.J., Withjack, M.O., 2010. A review of recent developments concerning the structure, mechanics and fluid flow properties of fault zones. J. Struct. Geol. 32, 1557–1575.

Federico, L., Spagnolo, C., Crispini, L., Capponi, G., 2009. Fault-slip analysis in the metaophiolites of the Voltri Massif: constraints for the tectonic evolution at the Alps/Apennine boundary. Geol. J. 44, 225–240.

Federico, L., Crispini, L., Vigo, A., Capponi, G., 2014. Unravelling polyphase brittle tectonics through multi-software fault-slip analysis: the case of the Voltri Unit, Western Alps (Italy). J. Struct. Geol. 68, 175–193.

Fondriest, M., Mecklenburgh, J., Passelegue, F.X., Artioli, G., Nestola, F., Spagnuolo, E., et al., 2020. Pseudotachylyte alteration and the rapid fade of earthquake scars from the geological record. Geophys. Res. Lett. 47 (22), e2020GL090020.

Fondriest, M., Smith, S.A.F., Di Toro, G., Zampieri, D., Mittempergher, S., 2012. Fault zone structure and seismic slip localization in dolostones, an example from the Southern Alps, Italy. J. Struct. Geol. 45, 52–67.

Fossen, H., 2016. Fracture and Brittle Deformation Structural Geology, second ed. ed. Cambridge University Press, pp. 124–149.
Fournier, R.O., 1985. The behaviour of silica in hydrothermal solutions. In: Robertson, J. M. (Ed.), Geology and Geochemistry of Epithermal Systems. Society of Economic Geologist, pp. 45–61.
Frenzel, M., Woodcock, N.H., 2014. Cockade breccia: product of mineralisation along dilational faults. J. Struct. Geol. 68, 194e206, 2014.
Fusswinkel, T., Wagner, T., Sakellaris, G., 2017. Fluid evolution of the Neoarchean Pampalo orogenic gold deposit (E Finland): constraints from LA-ICPMS fluid inclusion microanalysis. Chem. Geol. 450, 96–121.
Garofalo, P.S., Fricker, M.B., Guenther, D., Bersani, D., Lottici, P.P., 2014. Physical-chemical properties and metal budget of Au-transporting hydrothermal fluids in orogenic deposits. In: Garofalo, P.S., Ridley, J.R. (Eds.), Gold-transporting Hydrothermal Fluids in the Earth's Crust. Special Publication 402. The Geological Society of London, London, pp. 71–102.
Garofalo, P.S., Scarsi, M., Gundlach-Graham, A., Schwarz, G., Günther, D., 2023. Feedbacks between fast brittle faulting, hydrothermal fluid flow, and metal transport within carbonated ultramafics (Ligurian Western Alps, Italy). Miner. Deposita 58, 833–852. https://doi.org/10.1007/s00126-022-01142-y.
Gelati, R., Gnaccolini, M., 1988. Sequenze deposizionali in un bacino episuturale, nella zona di raccordo tra Alpi ed Appennino Settentrionale. Atti Ticinensi Sci. della Terra 31, 340–350.
Genna, A., Jébrak, M., Marcoux, E., Milési, J.P., 1996. Genesis of cockade breccias in the tectonic evolution of the Cirotan epithermal gold system, West Java. Can. J. Earth Sci. 33, 93–102.
Giorza, A., 2010. Late to post-metamorphic hydrothermalism in the Voltri Unit (Lavagnina Lakes Area, NW Alps). Structural-Petrological-Geochemical Approach, Dipartimento di Scienze della Terra. Università degli Studi di Torino, Torino, Italy, p. 240.
Gránásy, L., Pusztai, T., Tegze, G., Warren, J.A., Douglas, J.F., 2005. Growth and form of spherulites. Phys. Rev. 72 (72), 011605.
Gudmundsson, A., Simmenes, T.H., Larsen, B., Philipp, S.L., 2010. Effects of internal structure and local stresses on fracture propagation, deflection, and arrest in fault zones. J. Struct. Geol. 32, 1643–1655.
Halls, C., Zhao, R., 1995. Listvenite and related rocks: perspectives on terminology and mineralogy with reference to an occurrence at Cregganbaun, Co. Mayo, Republic of Ireland. Miner. Deposita 30, 303–313.
Hayward, K.S., Cox, S.F., Fitz Gerald, J.D., Slagmolen, B.J.J., Shaddock, D.A., Forsyth, P. W.F., Salmon, M.L., Hawkins, R.P., 2016. Mechanical amorphization, flash heating, and frictional melting: dramatic changes to fault surfaces during the first millisecond of earthquake slip. Geology 44, 1043–1046.
Hu, J., Duan, Z., Zhu, C., Chou, I.M., 2007. PVTx properties of the CO2–H2O and CO2–H2O–NaCl systems below 647 K: Assessment of experimental data and thermodynamic models. Chem. Geol. 238, 249–267.
Hu, H., Brovarone, A.V., Zhang, L., Piccoli, F., Peng, W., Shen, T., 2021. Retrograde carbon sequestration in orogenic complexes: a case study from the Chinese southwestern Tianshan. Lithos 392, 106151.
Kaszuba, J.P., Williams, L.L., Janecky, D.R., Hollis, W.K., Tsimpanogiannis, I.N., 2006. Immiscible CO2-H2O fluids in the shallow crust. G-cubed 7 (10).
Kaduri, M., Gratier, J.-P., Renard, F., Çakir, Z., Lasserre, C., 2017. The implications of fault zone transformation on aseismic creep: example of the North Anatolian Fault, Turkey. J. Geophys. Res. Solid Earth 122. https://doi.org/10.1002/2016JB013803.
Kelemen, P.B., Matter, J., Streit, E.E., Rudge, J.F., Curry, W.B., Blusztajn, J., 2011. Rates and mechanisms of mineral carbonation in peridotite: natural processes and recipes for enhanced, in situ CO2 capture and storage. Annu. Rev. Earth Planet Sci. 39, 545–576.
Kim, Y.-S., Peacock, D.C.P., Sanderson, D.J., 2004. Fault damage zones. J. Struct. Geol. 26, 503–517.
Kim, J.H., Ree, J.H., Hirose, T., Oohashi, K., 2022. Formation of clast-cortex aggregates in experimental fault gouges. Tectonophysics 839, 229524.
Kirkpatrick, J.D., Rowe, C.D., White, J.C., Brodsky, E.E., 2013. Silica gel formation during fault slip: evidence from the rock record. Geology 41, 1015–1018.
Kirkpatrick, J.D., Rowe, C.D., 2013. Disappearing ink: how pseudotachylytes are lost from the rock record. J. Struct. Geol. 52, 183–198.
Kuo, L.-W., Song, S.-R., Suppe, J., Yeh, E.-C., 2016. Fault mirrors in seismically active fault zones: a fossil of small earthquakes at shallow depths. Geophys. Res. Lett. 43, 1950–1959.
Laubscher, H., Biella, G.C., Cassinis, R., Gelati, R., Lozej, A., Scarascia, S., Tabacco, I., 1992. The collisional knot in Liguria. Geol. Rundsch. 81, 275–289.
Lin, A., 1994. Glassy pseudotachylyte veins from the Fuyun fault zone, northwest China. J. Struct. Geol. 16 (1), 71–83.
Locatelli, M., Verlaguet, A., Agard, P., Pettke, T., Federico, L., 2019. Fluid pulses during stepwise brecciation at intermediate subduction depths (Monviso eclogites, W. Alps): first internally then externally sourced. G-cubed 20 (11), 5285–5318.
Locatelli, M., Verlaguet, A., Agard, P., Federico, L., Angiboust, S., 2018. Intermediate-depth brecciation along the subduction plate interface (Monviso eclogite, W. Alps). Lithos 320, 378–402.
Maino, M., Decarlis, A., Felletti, F., Seno, S., 2013. Tectono-sedimentary evolution of the tertiary Piedmont Basin (NW Italy) within the oligo–miocene central mediterranean geodynamics. Tectonics 32 (3), 593–619.
Manna, L., Perozzo, M., Menegoni, N., et al., 2023. Anatomy of a km-scale fault zone controlling the Oligo-Miocene bending of the Ligurian Alps (NW Italy): integration of field and 3D high-resolution digital outcrop model data. Swiss J. Geosci. 116, 15. https://doi.org/10.1186/s00015-023-00444-.
Mariani, E., Mecklenburgh, J., Wheeler, J., Prior, D.J., Heidelbach, F., 2009. Microstructure evolution and recrystallization during creep of MgO single crystals. Acta Mater. 57 (6), 1886–1898.
Masoch, S., Fondriest, M., Preto, N., Secco, M., Di Toro, G., 2019. Seismic cycle recorded in cockade-bearing faults (Col de Teghime, Alpine Corsica). J. Struct. Geol. 129, 103889.
Micklethwaite, S., 2009. Mechanisms of faulting and permeability enhancement during epithermal mineralisation: cracow goldfield, Australia. J. Struct. Geol. 31, 288–300.
Moncada, D., Mutchler, S., Nieto, A., Reynolds, T.J., Rimstidt, J.D., Bodnar, R.J., 2012. Mineral textures and fluid inclusion petrography of the epithermal Ag–Au deposits at Guanajuato, Mexico: application to exploration. J. Geochem. Explor. 114, 20–35.
Moore, D.E., Rymer, M.J., 2007. Talc bearing serpentinite and the creeping section of the San Andreas fault. Nature 448 (7155), 795–797. https://doi.org/10.1038/nature06064.
Moore, D.E., Lockner, D.A., 2013. Chemical controls on fault behavior: weakening of serpentinite sheared against quartz-bearing rocks and its significance for fault creep in the San Andreas system. J. Geophys. Res. Solid Earth 118, 2558–2570.
Morelli, D., Locatelli, M., Crispini, L., Corradi, N., Cianfarra, P., Federico, L., Brandolini, P., 2023. 3D modelling of late quaternary coastal evolution between albenga and loano (Western Liguria, Italy). J. Maps 19 (1), 2227211.
Morelli, D., Locatelli, M., Corradi, N., Cianfarra, P., Crispini, L., Federico, L., Migeon, S., 2022. Morpho-structural setting of the Ligurian Sea: the role of structural heritage and neotectonic inversion. J. Mar. Sci. Eng. 10 (9), 1176.
Mueller, P., Tamburelli, S., Menegoni, N., Perozzo, M., Amadori, C., Crispini, L., et al., 2023. Concurrence of load-and-flame structures, balls-and-pillows, clastic injectites and shear deformation bands as indicator of seismicity in mixed siliciclastic-carbonate successions (Finale Ligure Basin, Italy). Mar. Petrol. Geol. 155, 106345.
Nader, F.H., 2007. Petrographic and geochemical study on cave pearls from Kanaan Cave (Lebanon). Int. J. Speleol. 36 (1), 4.
Nakamuro, T., Sakakibara, M., Nada, H., Harano, K., Nakamura, E., 2021. Capturing the moment of emergence of crystal nucleus from disorder. J. Am. Chem. Soc. 143 (4), 1763–1767.
Niemeijer, A., Di Toro, G., Griffith, W.A., Bistacchi, A., Smith, S.A.F., Nielsen, S., 2012. Inferring earthquake physics and chemistry using an integrated field and laboratory approach. J. Struct. Geol. 39, 2–36.
Otsuki, K., Hirono, T., Omori, M., Sakaguchi, M., Tanigawa, W., Lin, W., et al., 2009. Analyses of pseudotachylyte from hole-B of Taiwan chelungpu fault drilling project (TCDP); their implications for seismic slip behaviors during the 1999 chi-chi earthquake. Tectonophysics 469 (1–4), 13–24.
Passchier, C.W., Trouw, R.A.J., 2005. Microtectonics, second ed. Springler-Verlag, Berlin, Heidelberg.
Piccoli, F., Brovarone, A.V., Beyssac, O., Martinez, I., Ague, J.J., Chaduteau, C., 2016. Carbonation by fluid–rock interactions at high-pressure conditions: implications for carbon cycling in subduction zones. Earth Planet Sci. Lett. 445, 146–159.
Pipino, G., 2003. Oro, Miniere, Storia. Miscellanea di giacimentologia e storia mineraria italiana. Museo storico dell'oro italiano Ed., pp. 510.
Prior, D.J., Boyle, A.P., Brenker, F., Cheadle, M.C., Day, A., Lopez, G., et al., 1999. The application of electron backscatter diffraction and orientation contrast imaging in the SEM to textural problems in rocks. Am. Mineral. 84 (11–12), 1741–1759.
Prior, D.J., Mariani, E., Wheeler, J., 2009. EBSD in the earth sciences: applications, common practice, and challenges. In: Electron Backscatter Diffraction in Materials Science, pp. 345–360.
Ramsey, J.M., Chester, F.M., 2004. Hybrid fracture and the transition from extension fracture to shear fracture. Nature 428 (6978), 63–66. https://doi.org/10.1038/nature02333. PMID: 14999 279.
Ramsay, J.G., Huber, M.I., 1987. Ductile and Brittle Shear Zones, the Techniques of Modern Structural Geology. Academic Press, London, UK, pp. 595–640.
Reed, M.H., 1997. Hydrothermal alteration and its relationships to ore fluid composition. In: Barnes, H.L. (Ed.), Geochemistry of Hydrothermal Ore Deposits, third ed. John Wiley & Sons, Inc., pp. 303–365
Rempe, M., Smith, S.A.F., Ferri, F., Mitchell, T.M., Di Toro, G., 2014. Clast-cortex aggregates in experimental and natural calcite-bearing fault zones. J. Struct. Geol. 68, 142–157.
Rice, J.R., 1992. Fault stress states, pore pressure distributions, and the weakness of the San Andreas fault. In: Evans, B., Wong, T.-F. (Eds.), Fault Mechanics and Transport Properties of Rock, Int. Geophys. Ser., vol. 51. Academic, San Diego, Calif, pp. 475–503. https://doi.org/10.1016/S0074-6142(08)62835-1.
Ridley, J.R., Diamond, L.W., 2000. Fluid chemistry of orogenic lode-gold deposits and implications for genetic models. In: Hagemann, S.G., Brown, P.E. (Eds.), Gold in 2000. Society of Economic Geologist, Inc., pp. 141–162
Rodriguez-Blanco, J.D., Sand, K.K., Benning, L.G., 2017. ACC and vaterite as intermediates in the solution-based crystallization of CaCO3. In: Van Driessche, A.E. S., Kellermeier, M., Benning, L.G., Gebauer, D. (Eds.), New Perspectives on Mineral Nucleation and Growth. From Solution Precursors to Solid Materials. Springer, pp. 93–111.
Rogowitz, A., White, J.C., Grasemann, B., 2016. Strain localization in ultramylonitic marbles by simultaneous activation of dislocation motion and grain boundary sliding (Syros, Greece). Solid Earth 7 (2), 355–366.
Rollet, N., Déverchere, J., Beslier, M.O., Guennoc, P., Réhault, J.P., Sosson, M., Truffert, C., 2002. Back arc extension, tectonic inheritance, and volcanism in the Ligurian Sea, Western Mediterranean. Tectonics 21 (3), 6, 1.
Rowe, C.D., Fagereng, Å., Miller, J.A., Mapani, B., 2012. Signature of coseismic decarbonation in dolomitic fault rocks of the Naukluft Thrust, Namibia. Earth Planet Sci. Lett. 333–334, 200–210.
Rowe, C.D., Griffith, W.A., 2015. Do faults preserve a record of seismic slip: a second opinion. J. Struct. Geol. 78, 1–26.

Rudnick, R.L., Gao, S., 2003. The composition of the continental crust. In: Holland, H.D., Turekian, K.K. (Eds.), Treatise on Geochemistry. Volume 3. The Crust. Elsevier, pp. 1–64.
Rutter, E.H., Maddock, R.H., Hall, S.H., White, S.H., 1986. Comparative microstructures of natural and experimentally produced clay bearing fault gouges. Pure Appl. Geophys. 124, 3–30. https://doi.org/10.1007/BF00875717.
Sant'Anna, L.G., Riccomini, C., Rodrigues-Francisco, B.H., Sial, A.N., Carvalho, M.D., Moura, C.A.V., 2004. The Paleocene travertine system of the Itaboraí basin, Southeastern Brazil. J. S. Am. Earth Sci. 18 (1), 11–25.
Scambelluri, M., Strating, E.H., Piccardo, G.B., Vissers, R.L.M., Rampone, E., 1991. Alpine olivine-and titanian clinohumite-bearing assemblages in the Erro-Tobbio peridotite (Voltri Massif, NW Italy). J. Metamorph. Geol. 9 (1), 79–91.
Scambelluri, M., Rampone, E., Piccardo, G.B., 2001. Fluid and element cycling in subducted serpentinite: a trace-element study of the erro-tobbio high-pressure ultramafites (Western Alps, NW Italy). J. Petrol. 42, 55–67.
Scarsi, M., 2018. Faulting, fluid-rock interaction and hydrothermal mineralisation in ultramafic rocks (Voltri Massif, Ligurian Alps), PHD Thesis. University of Genova 280.
Scarsi, M., Crispini, L., Malatesta, C., Spagnolo, C., Capponi, G., 2019. Geological map of a treasure chest of geodiversity: the Lavagnina Lakes area (Alessandria, Italy). Geosciences 9 (5), 229. https://doi.org/10.3390/geosciences9050229.
Shelly, D.R., Taira, T.a., Prejean, S.G., Hill, D.P., Dreger, D.S., 2015. Fluid-faulting interactions: fracture-mesh and fault-valve behavior in the February 2014 Mammoth Mountain, California, earthquake swarm. Geophys. Res. Lett. 42, 5803–5812.
Shtukenberg, A.G., Punin, Y.O., Gunn, E., Kahr, B., 2012. Spherulites. Chemical reviews 112 (3), 1805–1838.
Sibson, R.H., 1977. Fault rocks and fault mechanisms. J. Geol. Soc. 133, 191–213.
Sibson, R.H., 1981. Fluid flow accompanying faulting: field evidence and models. In: Simpson, D.W., Richards, P.G. (Eds.), Earthquake Prediction. American Geophysical Union, pp. 593–603.
Sibson, R.H., 1986. Earthquakes and rock deformation in crustal fault zones. Annu. Rev. Earth Planet Sci. 14 (1), 149–175.
Sibson, R.H., 1992. Implications of fault-valve behaviour for rupture nucleation and recurrence. Tectonophysics 211, 283–293.
Sibson, R.H., 2001. Seismogenic framework for hydrothermal transport and ore deposition. In: Richards, J.P., Tosdal, R.M. (Eds.), Structural Control on Ore Genesis. Society of Economic Geologists, pp. 25–50.
Sibson, R.H., Robert, F., Poulsen, K.H., 1988. High angle reverse faults, fluid pressure cycling, and mesothermal gold-quartz deposits. Geology 16, 551–555.
Smith, S.A.F., Faulkner, D., 2010. Laboratory measurements of the frictional properties of the Zuccale low-angle normal fault, Elba Island, Italy. J. Geophys. Res. 115 https://doi.org/10.1029/2008JB006274.
Smith, S.A., Billi, A., Di Toro, G., Spiess, R., 2011. Principal slip zones in limestone: microstructural characterization and implications for the seismic cycle (Tre Monti Fault, Central Apennines, Italy). Pure Appl. Geophys. 168, 2365–2393.
Smye, A.J., Seman, S.M., Scambelluri, M., Starr, P.G., Federico, L., 2021. Exhumation dynamics of high-pressure metamorphic rocks from the Voltri Unit, Western Alps: constraints from phengite Rb–Sr geochronology. Contrib. Mineral. Petrol. 176 (2), 14, 2021.
Spagnolo, C., Crispini, L., Capponi, G., 2007. Late structural evolution in an accretionary wedge: insights from the Voltri Massif (Ligurian Alps, Italy). Geodin. Acta 20/1–2, 21–35.
Speckbacher, R., Behrmann, J.H., Nagel, T.J., Stipp, M., Devey, C.W., 2011. Splitting a continent: insights from submarine high resolution mapping of the Moresby Seamount detachment, offshore Papua New Guinea. Geology 39 (7), 651–654. https://doi.org/10.1130/G31931.1.
Speckbacher, R., Behrmann, J.H., Nagel, T.J., Stipp, M., Mahlke, J., 2012. Fluid flow and metasomatic fault weakening in the Moresby Seamount detachment, Woodlark Basin, offshore Papua New Guinea. G-cubed 13 (11).
Sunagawa, I., 1978. Vapour growth and epitaxy of minerals and synthetic crystals. J. Cryst. Growth 45, 3–12.
Swanson, M.T., 1988. Pseudotachylyte-bearing strike-slip duplex structures in the fort foster brittle zone, S. Maine. J. Struct. Geol. 10 (8), 813–828.
Van Noort, R., Spiers, C.J., Drury, M.R., Kandianis, M.T., 2013. Peridotite dissolution and carbonation rates at fracture surfaces under conditions relevant for in situ mineralization of CO2. Geochem. Cosmochim. Acta 106, 1–24.
Vanossi, M., Perotti, C.R., Seno, S., 1994. The maritime Alps arc in the Ligurian and tyrrhenian systems. Tectonophysics 230 (1–2), 75–89.
Vignaroli, G., Rossetti, F., Rubatto, D., Theye, T., Lisker, F., Phillips, D., 2010. - pressure-temperature-deformation-time (P-T-d-t) exhumation history of the Voltri Massif HP complex, Ligurian Alps, Italy. Tectonics 29, TC6009. https://doi.org/10.1029/2009TC002621.
Wang, H., Li, H.B., Di Toro, G., Kuo, L.W., Spagnuolo, E., Aretusini, S., et al., 2023. Melting of fault gouge at shallow depth during the 2008 MW 7.9 Wenchuan earthquake, China. Geology 51 (4), 345–350.
Wang, H.L., Xu, W.Y., Shao, J.F., 2014. Experimental researches on hydro-mechanical properties of altered rock under confining pressures. Rock Mech. Rock Eng. 47, 485–493.
Whitney, D.L., Evans, B.W., 2010. Abbreviations for names of rock-forming minerals. Am. Mineral. 95, 185–187.
Wu, C., Yi, H., Hui, B., Xia, G., Ma, X., 2014. A new sediment type of coated grain: oolitic sinter. Sci. China Earth Sci. 57 (9), 2013–2024.
Yuan, F., Prakash, V., Tullis, T., 2011. Origin of pulverized rocks during earthquake fault rupture. J. Geophys. Res. Solid Earth 116.